Abstract

The abstract for your chapter is reproduced below for your reference. Please note that this will **not** appear in the final printed version of your chapter.

Branched metallic nanocrystals have an array of useful properties that can be customized through parameters like shape, size, and composition. In most cases, the shape or morphology of a metallic nanostructure plays the most critical role in determining its properties and suitability for certain applications. In recent years, there has been growing interest in using anisotropic metal nanostructures for photothermal applications. This has lead to greater development in their optical properties as well as synthetic methods that are non-toxic and biocompatible. In this book chapter, various traditional and modern synthetic methods to obtain metal nanostructures with branched morphologies will be discussed in detail. The properties of these materials will also be explored, with the focus on optical properties that lead to their photothermal applications. The recent developments of the photothermal applications are also reviewed. And lastly, an outlook on the research area is also presented.

CHAPTER 3

Branched Metallic Nanocrystals: Synthesis, Properties, and Photothermal Applications

KAREN YUANTING TANG,[a] JERRY ZHI XIONG HENG,[a] KHIN YIN WIN,[b] SI YIN TEE,[a] ZIBIAO LI*[a,c] AND ENYI YE*[a]

[a] Institute of Materials Research and Engineering, Agency for Science, Technology & Research, 2 Fusionopolis Way, Singapore 138634, Singapore; [b] Singapore Institute of Food and Biotechnology Innovation, Agency for Science, Technology & Research, 31 Biopolis Way, Singapore 138669, Singapore; [c] Department of Materials Science and Engineering, National University of Singapore, 9 Engineering Drive 1, Singapore 117576, Singapore
*Emails: lizb@imre.a-star.edu.sg; yeey@imre.a-star.edu.sg

3.1   Introduction

Metal nanostructures have distinctive and captivating properties which enable them to be used in an extensive range of applications across multiple research disciplines. The size and shape of such materials are crucial parameters that affect their properties and specific functions for different applications. In many cases, shape offers much better flexibility in tuning the properties of metal nanostructures as different nanocrystal shapes exhibit different physical and chemical properties. For example, the surface plasmon resonance (SPR) characteristics of gold nanoparticles can change dramatically due to their different shapes, resulting in a change in color.[1] This can give rise to various applications like sensing, imaging, surface-enhanced Raman scattering, and

photothermal therapy.[2–4] The type of facets exposed on the surface also affects
the catalytic activity and selectivity of Pt and Pd nanoparticles.[5,6] This has
gained great interest and been used in major catalytic reactions, such as the
oxygen reduction reaction and formic acid oxidation.[3] Different bactericidal
properties of silver nanostructures against *E. coli* due to shape variation have
also been reported.[7] Synthesis of metal nanostructures with controllable
shapes had become an extensive area of research, as the demand for specific
metal nanostructures with a particular morphology grows.

Nanostructured metals with controlled morphologies can be easily prepared
as colloids through wet-chemical synthetic methods. For the past century,
synthetic protocols have been developed for preparations of colloidal metal
nanostructures with various shapes, dating back to 1857, when spherical Au
nanoparticles were synthesized and documented.[8] But it was not until the last
two decades that fabrication of highly complex geometrical metal nanostruc-
tures was achieved. Of all synthetic methods, the solution-based approach to
synthesize nanocrystals emerged, as it is able to produce nanostructures with a
wide variety of shapes, from simple geometries like rods and cubes, to more
complicated morphologies like cages and highly branched architectures.[9–12]

In this book chapter, we will be focusing on metallic nanostructures with
anisotropically branched morphologies. This is a special class of metal
nanostructures, which can be effectively modified to suit the various appli-
cations. We will discuss the various synthesis strategies of these anisotropic
branched metallic nanostructures in Section 3.2. We will investigate how the
morphologies affect the optical properties in Section 3.3, and the various
photothermal therapeutic applications in Section 3.4. Lastly, the conclusions
and a future perspective are appended in the final section.

3.2 Strategies for the Synthesis of Anisotropic Branched Metallic Nanostructures

Through appropriate choice of the synthetic method and finetuning of the
experimental conditions, one can obtain nanostructured materials of the
targeted size and shape. For branched metallic nanostructures, the mech-
anism of branch formation depends greatly on the type of synthetic ap-
proach used. In this section, we focus on the different synthetic protocols
based on wet chemistry, which have been reported to successfully prepare
anisotropic branched metallic nanostructures. We classify the protocols into
5 main strategies, (1) seeded growth, (2) seedless growth, (3) templated
growth, (4) chemical etching, and (5) green methods.

3.2.1 Seeded Growth

The seeded growth methodology is one of the approaches used in traditional
crystal growing.[13] It utilizes pre-synthesized seeds as nucleation points for
growth of anisotropic branched metallic nanostructures. This method re-
quires an additional step of synthesis, as it distinctly separates the nucleation

event from the growth. This separation might be considered as inconvenient, but it allows precise control of the size of the nanocrystals.[14] The morphology of the targeted nanostructures can also be controlled with the change of size, shape, and composition of the seeds, with this strategy.

One of the classical examples of the seeded growth methodology is by reducing $HAuCl_4$ in the presence of cetyl-trimethylammoinium bromide (CTAB) as a surfactant and silver salt, to form gold nanorods. A thin layer of silver bromide (from silver salt with CTAB) is formed epitaxially on Au {111} and promotes the growth of gold nanorods with {111} facets. Through careful tuning of the concentration of the different reagents, Murphy's group was able to synthesize short Au nanorods, ranging from 20 to 100 nm (aspect ratio from 2 to 4) in high yield.[15,16]

Xia and co-workers[17] also reported the successful formation of Au nano-hexapods from Au nanocrystal seeds. They synthesized the gold nanohexapods by reducing $HAuCl_4$ using dimethylformamide (DMF) in water, in the presence of octahedral-shaped Au seeds. The Au atoms nucleated and grew favorably from the 6 vertices of the nano-octahedra, forming the Au nanohexapods. The arm lengths of the nanohexapods can be controlled by varying certain experimental parameters such as temperature and the amount of $HAuCl_4$ added. Another group, Skrabalak *et al.*[18–20] managed to produce an Au–Pd bimetallic nanocrystal that has an Au-rich interior with Pd-rich exterior (Figure 3.1A). This was done by co-reduction of $HAuCl_4$ and H_2PdCl_4 using ascorbic acid, in the presence of pre-synthesized Au nano-octahedra. As the reduction potential of $HAuCl_4$ is higher than H_2PdCl_4, Au was deposited on the Au seeds first, followed by the deposition of Pd at the tip of the branches. Interestingly, the branches grow from the eight {111}c facets, rather than the 6 vertices, as mentioned above. Through further investigation, the octahedral Au seeds undergo restructuring to form a cubic structure before the formation of the arms. Hence, the eight branches were grown from the eight vertices of the intermediate cubic structure. Another noteworthy observation is that the morphology of the bimetallic nanocrystal can be tuned by a simple change in the pH, resulting in nano-octapods, concave nanostructures, and nano-octahedra.

Stabilizers like poly(vinylpyrrolidone) (PVP) are also sometimes used in the synthesis of branched anisotropic nanostructures. The addition of PVP controls the reduction kinetics of $AuCl_4^-$ ions on the Au seed surfaces. Hence, the rapid, kinetically controlled growth along the preferred crystal facets enables the formation of branched Au nanostructures with pointed tips. For example, gold nanostars can be obtained through this method, through careful control of PVP and DMF ratio.[21,22] Khoury and co-worker[22] reported the use of PVP and DMF with $HAuCl_4$ to obtain high-yield gold nanostars. Figure 3.1B shows the growth of the nanostars from the gold seeds. They suggested that the growth mechanism involves two stages: first, a rapid growing phase after nucleation of Au seeds. This rapid growth phase allows the formation of shallow protrusions that originate from the surface and develop distinct branches. Second, a gradual growth which mainly involves the deposition of gold on the protrusions, forming the branches of the nanostars.
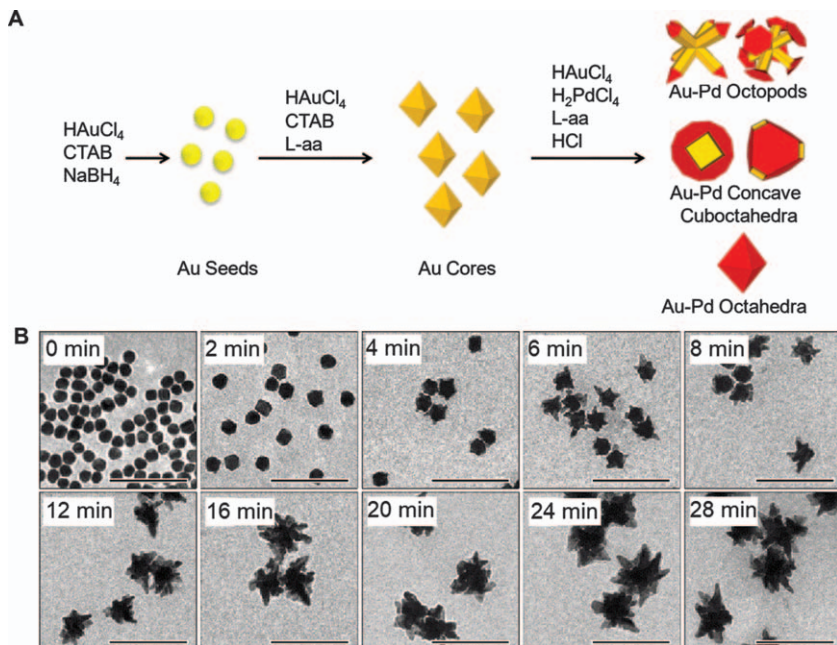
Figure 3.1   Seeded growth of anisotropically branched metal nanocrystals. (A) Schematic representation that illustrates the synthesis of Au–Pd nanocrystals from Au seeds. Adapted from ref. 19 with permission from American Chemical Society, Copyright 2014. (B) TEM images of nanostar formation over time. Reproduced from ref. 22 with permission from American Chemical Society, Copyright 2008.

3.2.2   Seedless Growth

Seedless growth is also another commonly used strategy for anisotropic branching of metal nanostructures. It has gained its popularity due to its facile one-pot approach, as well as its high versatility and capability. However, the size and morphology of the nanostructures may be affected by the *in situ* formation of the metal core and subsequent branching, as the rates of nucleation and growth compete with each other. Another critical challenge is the need to break the highly symmetrical fcc structure of metals for the formation of these anisotropically branched structures. In this subsection, we will discuss how twin defects, ions, ligands, and polymorphs have been used to facilitate the growth of such nanostructures *via* the seedless route.

3.2.2.1   *Twin-determined Branching*

A twinned crystal is formed when two or more separate crystals intergrow together symmetrically. This could happen when there is erroneous attachment of adatoms, resulting in crystals separated by the twin boundary. Metals with low stacking fault energy are most vulnerable to twinning. For example, fcc metals are more prone to forming thermodynamically favored

nanocrystals with five-fold symmetry in very small sizes. However, the twinned structure should not be sustained when the crystal grows bigger, due to the dramatic increase of the strain energy, and single crystal structures like truncated octahedrons are formed. With careful manipulation and control of the growth conditions, a wide array of shapes can also be obtained at larger sizes.

Yang and co-workers[23] explored the roles of twin defects in the formation of platinum multipod nanostructures. They determined that the number of twinned planes formed at the initial stage of crystal growth will affect the final morphology of the Pt nanostructures. Without the twin plane, the initial cuboctahedral nanocrystals evolve slowly into octapods under conditions promoting growth along the $\langle 111 \rangle$ directions (Figure 3.2(i)). However, the presence of twin planes in the initial nanocrystal leads to different end morphologies. In Figure 3.2(ii)–(iv), the initial nanocrystals with single, five-fold, and multiply twinned planes transform into planar tripods, multipod structures with a rod like center, and monopod/multipod structures with a sphere-like core, respectively. Notably, the twining events and growth kinetics along the given directions can be drastically altered by changing the
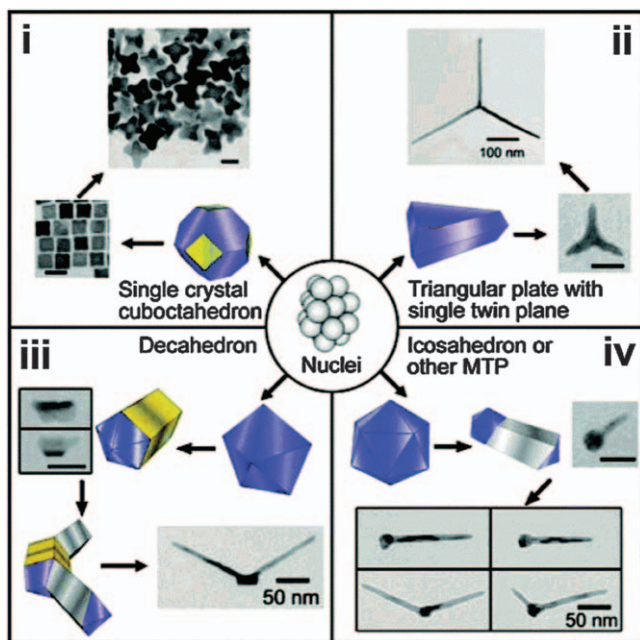

Figure 3.2 Twin-determined branching. Schematic illustration that shows the evolution of Pt nuclei to nanostructures with various branched morphologies. The number of twin planes in the initially formed nanocrystals is the determinant of the final morphology of the nanocrystal.
Reproduced from ref. 23 with permission from American Chemical Society, Copyright 2007.

reaction conditions (*e.g.* reaction temperature). This can trigger formation of various branched nanostructures.

Xia's group[24] showed that the five-fold twinned Rh decahedral structure that was formed initially evolved into a starfish-like morphology under desirable conditions. Using $[\{Rh(CF_3COO)_2\}_2]$ as the Rh precursor, ethylene glycol as the reductant and PVP as stabilizers, the reaction mixture is heated to 180 °C, and samples are collected at different intervals. At the initial stage, the Rh nanocrystals formed are multiply-twinned five-fold structures, mostly in a decahedron shape. The arms started to grow from the twin boundary corners along the $\langle 110 \rangle$ direction, with further heating. Interestingly, this is normally not observed in other noble metal systems, as the initial decahedral nanocrystals typically grow axially along the five-fold twin junction, forming elongated nanostructures, like nanorods and nanowires, with a pentagonal cross-section.[9,10,25] The preferred elongation is due to preferential binding of capping agents on the {100} facets of the growing nanostructures. However, in the Rh decahedral nanocrystals, the PVP is not able to effectively bind on the {100} side faces, hence, leading to a different growth behavior. It is also noteworthy that irregularly shaped nanocrystals are obtained instead of starfish-shaped ones when $[\{Rh(CF_3COO)_2\}_2]$ is replaced with Na_3RhCl_6 as the Rh precursor. The Cl ions in Na_3RhCl_6 will be released during the reaction and cause oxidative etching during the nucleation and growth processes when oxygen is present. This oxidative etching makes it difficult to obtain a twinned nanocrystal as twin defects are highly susceptible to oxidation and dissolution.

3.2.2.2   Ion-assisted Branching

Ion-assisted branching occurs whereby specific ions, which can be either cationic or anionic, are added to direct and mediate branching. Han *et al.*[26] used copper species as the reducing agent, instead of classical reducing agents such as citric acid or hydrazine, in the colloidal preparation of Au nanocrosses. The copper species also plays an important role during the nucleation stage. They direct the gold branches to grow along the $\langle 110 \rangle$ and $\langle 001 \rangle$ directions and secondary branching along $\langle 111 \rangle$, forming nanocrosses. With the careful choice of the Cu species, the size of the cross-shaped Au obtained can be controlled, due to the difference in the reduction rate. Cheng's group[27] revealed that spiky, urchin-like Au nanostructures can be obtained with the use of Ag^+ to induce branching, shown in Figure 3.3A. The Au nanostructures are produced from mixing $HAuCl_4$ and $AgNO_3$ with moderate amounts of ascorbic acid in water. The ascorbic acid favorably reduces $[AuCl_4]^-$, due to its higher reduction potential, to form Au nanocrystals. Small amounts of Ag^+ are then reduced and deposited on the surface of the Au nanocrystals. These Ag^0 atoms function as active sites and promote the growth of branches from the nanocrystals, resulting in the formation of anisotropic Au nanostructures. Fewer and larger spikes on the Au nanostructures can be observed when a decreasing amount of Ag^+ is
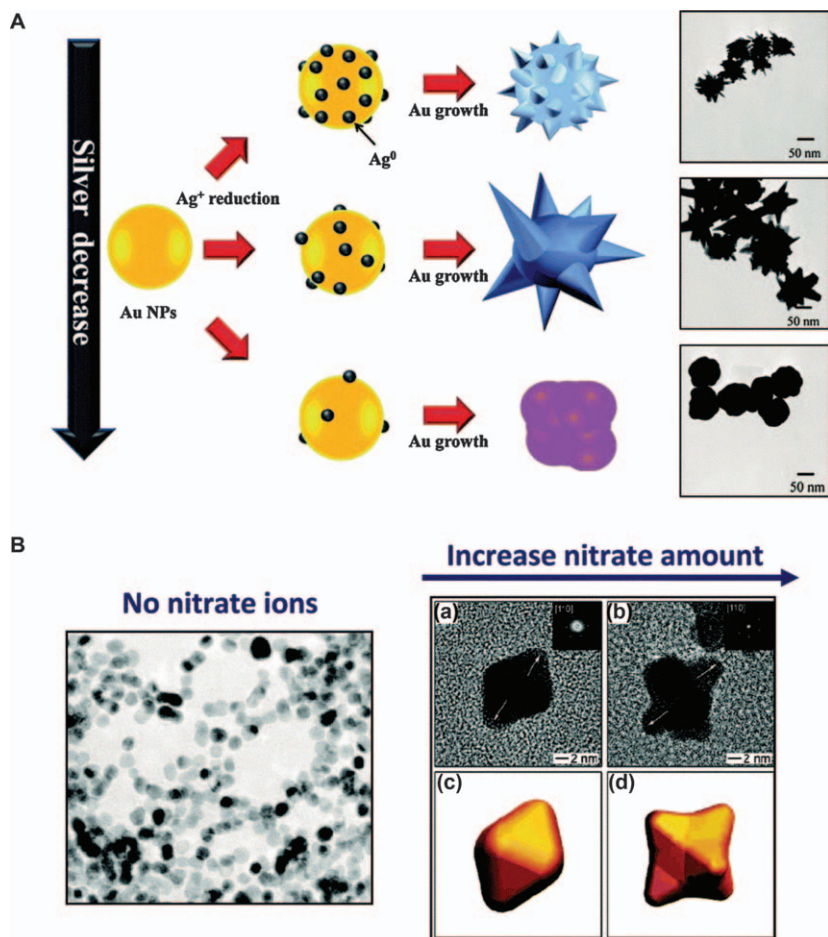
Figure 3.3 Ion-assisted branching. (A) Schematic illustration of the Ag^+-mediated growth of branched Au nanocrystals. By varying the Ag^+ concentration, the size and shape can be controlled. The TEM images of the resulting nanostructures are shown on the right. Reproduced from ref. 27 with permission from the Royal Society of Chemistry. (B) NO_3^- mediated growth of branched Pt nanocrystals. The TEM image on the left shows the spheroidal Pt nanocrystals that were obtained in the absence of NO_3^-. The effect of increasing the NO_3^- concentration is seen on the right. The HRTEM images (a and b) and the corresponding models (c and d) show that the growth of Pt nanocrystals was substantially enhanced at the ridges and corners to form multipods. Reproduced from ref. 28 with permission from American Chemical Society, Copyright 2004.

used. Conversely, when the Ag^+ concentration is too low, no spikes are obtained, resulting in popcorn-like nanostructures.

Other than cations, anions can also be used to assist in branching for anisotropic nanocrystals. Xia's group,[28] for instance, reported that the formation of such anisotropic Pt nanocrystals can be controlled by the addition

of nitrate ions (NO_3^-) to the polyol system. The concentration of nitrate ions
present in the system has a shape-directing effect, as shown in Figure 3.3B.
When no nitrate ions are present, only irregular spheroidal Pt nanocrystals
were obtained. As the concentration increases, the facets get more defined
and eventually, with sufficiently high concentrations, multipods are formed.
It was suggested that the Pt^{4+} reduction pathway was altered by the NO_3^-,
leading to the formation of anisotropic nanostructures. Absorption
spectroscopy data show that there is an *in situ* reduction of NO_3^- to NO_2^-,
which has a strong binding affinity with Pt ions, forming nitroplaninate
complexes. This substantially decelerates the reduction of Pt ions to Pt^0,
which alters the reaction kinetics and growth rates associated with different
crystallographic facets of the Pt nanostructures, resulting in anisotropically
branched nanostructures.

3.2.2.3   Ligand Directed Branching

Ligands (*e.g.* PVP) are well-known to be added to control the shape and sizes
of nanostructured materials. They have functional groups that can be
chemically bound to the nanocrystal structures. This binding helps to
facilitate the formation of branches, as it lowers the energy and slows the
growth rate of the bound facet relative to others. Zheng *et al.*[29] were able to
generate octapod-shaped Pt nanocrystals with exposed {411} high-index
facets by introducing a surface-controlling ligand, methylamine. Both PVP
and methylamine are used in the synthesis system as capping agents. When
only methylamine is present, highly aggregated Pt octapods are obtained,
showing that the main role of PVP is to prevent such aggregation of Pt
nanocrystals (Figure 3.4A). Meanwhile, when only PVP is used, mixed
morphologies of Pt nanocrystals are obtained, showing that methylamine
plays a crucial role in the octapod fabrication. Their results show that the
methylamine can bind selectively to the high-index {411} facets of Pt during
growth. The degree of concavity is also observed to be lowered significantly
when the amount of methylamine is reduced. Chen and co-workers[30]
showed that synthesis of Pd tetrapods is possible by using the amino acid
arginine. Arginine is able to favorably chemisorb on Pd {111} facets and
modifies the reduction kinetics of the Pd precursor.

   Tilley's group[31] was able to demonstrate that the final morphology of the
Pd nanocrystals can be modified through varying the nature of surface
capping ligands. The icosahedral Pd nanostructures were obtained when
oleylamine (OM) was used exclusively, suggesting that growth happens
thermodynamically. Yet when oleic acid (OA) is introduced with oleylamine
(1 : 1 ratio of OA : OM), anisotropically branched Pd nanostructures are
formed. As the carboxylic acid functionality of OA has weaker bonding to Pd
than the amine moiety of OM, the presence of OA destabilizes the system,
allowing kinetic growth of nanostructures, leading to branched morphology.
It is noted that the multipod arms grow in the direction where OA molecules
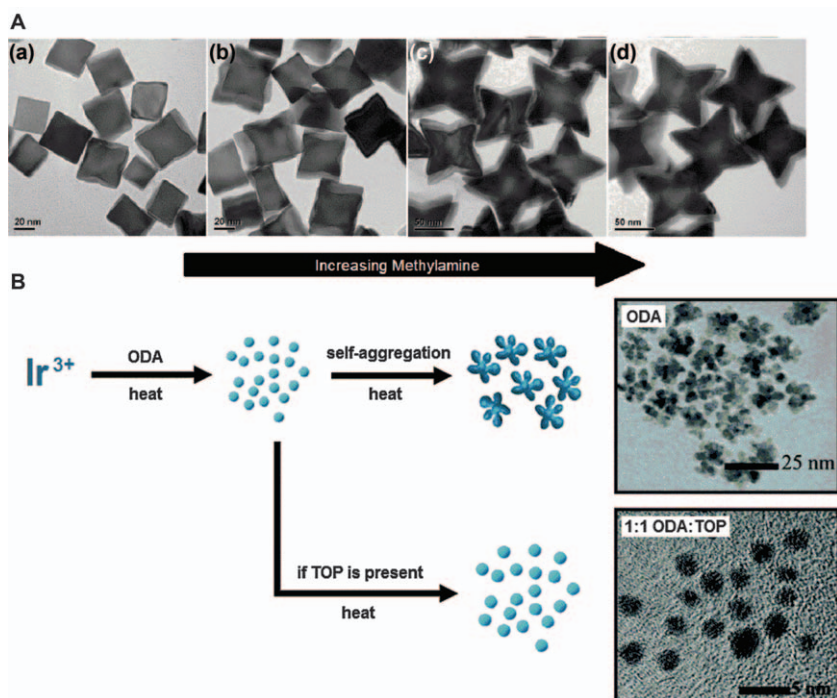bind themselves weakly to the faces of the structure.

Figure 3.4 Ligand-directed branching. (A) TEM images of Pt nanocrystals. The concavity of the Pt nanocrystals increases with more methylamine (ligand) added. Reproduced from ref. 29 with permission from American Chemical Society, Copyright 2011. (B) Schematic depiction and TEM images showing the ligand-controlled self-aggregation of Ir nanocrystals. Octadecylamine (ODA), a ligand with weak binding affinity toward Ir, promotes the self-aggregation of the weakly passivated Ir nanocrystals into nanodendrites. In the presence of trioctylphosphine (TOP), the growth of well-passivated quasi-spherical nanocrystals is favored. Reproduced from ref. 34 with permission from the Royal Society of Chemistry.

The biological buffer molecule, HEPES (2-[4-(2-hydroxyethyl)-1-piper-azinyl]ethanesulfonic acid), can be used as both a reducing and shape-directing agent to synthesize high yielding anisotropic Au nanostructures, as demonstrated by Lee *et al.*[32] The Au multipods fabricated have a selective tip growth along $\langle 111 \rangle$ directions. From the results, it is deduced that the piperazine group in HEPES is responsible for the adsorption of the molecule to the Au facets, binding most weakly at the {111} planes. Another study revealed that the HEPES molecules are able to self-assemble into long-range ordered structures at high concentrations, aiding the formation of branched Au nanostructures.[33] Based on theoretical calculations from experimental results, the HEPES molecule's sulfonate group preferably binds to the Au surface, and the free hydroxyl groups help with the self-assembly and bilayer formation through hydrogen bonding.

Choosing the appropriate ligands is also significant in the aggregation-based assembly of small metal nanocrystals into anistropically branched nanostructures. Ligands with weak to intermediate binding affinity to the metal ion precursor or small metal nanocrystals generally work best in forming highly branched nanostructures through this method. For example, formation of dendritic Ir nanocrystals is demonstrated by Zou and co-workers,[34] by using octadecylamine (ODA) as both the reductant and capping agent (Figure 3.4B). The Ir dendrites are synthesized simply by mixing $IrCl_3$ and ODA at 290 °C under a nitrogen flow for 15 minutes. Ir^{3+} was gradually reduced to Ir^0 at the initial stage of the reactions, enabling the formation of small Ir nanocrystals. With further heating, the Ir nanocrystals gradually self-aggregate and evolve into nanodendrites. The gradual reduction is regulated by ODA due to their weak binding affinity. As the stabilization by ODA is ineffective, Ir^0 coalescences and self-aggregates themselves into Ir nanocrystals. Only quasi-spherical Ir nanocrystals were obtained when a more effective stabilizer, trioctylphosphine (TOP), was added with ODA. The strong binding affinity of TOP enables the formation of a stable Ir^{3+} complex and delays the nucleation process due to ODA impeding the reduction of Ir^{3+}. Adding on, TOP enables the growth of nanocrystals to proceed through atomic addition rather than self-assembly due to its ability to effectively cap the surface of the initially formed nanocrystals. Such fabrication of aniso-tropically branched nanostructures through ligand-controlled self-aggregation is also reported in Pd nanodendrite synthesis.[35]

3.2.2.4   *Polymorphism-induced Branching*

When the solid metal compound exists in more than one crystalline form, polymorphism occurs. Hence, when the single crystal has more than one polymorph, growth will occur in different directions and branching occurs. Tilley's group[36] adopted the approach in synthesizing branched Ni nano-structures, exploiting Ni metal's inherent fcc–hcp polymorphism. Thermal decomposition and reduction of nickel acetylacetonate in mesitylene, in the presence of hexadecylamine (HDA) and trioctylphosphine (TOP) as capping ligands, under a hydrogen atmosphere, yield Ni nanostructures that consist of a fcc Ni core and alternating fcc and hcp phase arms. It is also noteworthy that the TOP ligand plays a crucial role in enhancing the growth of the branched structure. From the study, truncated octahedral fcc Ni nanocrystals are formed initially, which are bound by six {100} and eight {111} facets. Out of the 2 types of facets, growth occurs only with {111} facets due to the preferential binding of TOP molecules to the {100} facets, leading to arms formation. The {111} fcc facets will grow to become {001} hcp facets due to the presence of stacking faults along the [111] direction. Kinetic growth conditions, phase stability, and surface energies are some factors that are believed to contribute to the alternating fcc and hcp phases in the arms.

3.2.3   Templated Growth

Anisotropic branching of nanostructures can also be synthesized through a template-assisted growth approach. The template provides a structural scaffold for the nanostructures to grow into the templates' complementary shape. Xia *et al.*[37] successfully fabricated branched Au nanostructures by using an array of magnetic Fe nanoparticles as templates. From their study, it is shown that the Fe nanoparticles sis not only serves as a framework, but also plays a part in the reaction and falls apart naturally to release the desired product. The uniform quasi-spherical Fe nanoparticles self-assembled on a magnetic stir bar to form a three-dimensional (3D) porous lattice template. A galvanic replacement reaction between Fe and Au^+ takes place upon addition of AuCl, producing Au atoms. These Au atoms begin to nucleate and grow into multipods within the void spaces of the porous lattice. The magnetic attraction between the Fe nanoparticles is gradually weakened due to the consumption of Fe and the volume expansion from Au replacing Fe. This results in the eventual self-destruction of the template and releases the Au multipods naturally. Any residual Fe nanoparticles can be removed by acid washing of samples.

Liu and co-workers[38] reported the use of graphene oxide (GO) nanosheets as a scaffold to form highly branched Au nanostructures. GO is a two-dimensional (2D) honeycomb lattice of carbon atoms with various oxygen-containing moieties like carboxyl, hydroxyl, and epoxyl. *In situ* nucleation of Au atoms happens at these functionality sites during ethanol-assisted reduction. Subsequently, these oxygen-containing moieties also aid in directing the growth of the nanostructures, leading to a well-defined structure being formed. Only irregular Au nanocrystals, without a well-defined structure, were obtained when GO nanosheets were absent. Maroneze's group[39] also successfully obtained asymmetrical 2D gold nanostructures by using GO nanosheets as a template (Figure 3.5). The GO was first treated with cationic alkoxysilane to allow for adsorption of $AuCl_4^-$ onto GO, followed by *in situ* reduction of $AuCl_4^-$ to form Au nanoparticles, which then grow along the GO to form anisotropic 2D Au nanostructures. When the reaction proceeds, the nanostructures get larger and start to coalesce together to form a complete layer, resulting in anisotropic nanosheets. One issue noted is that these Au nanosheets contain some defects, such as holes and slits, as a result of a coalescence process.

Another template that has been used for this kind of synthesis in solution is deep eutectic solvent (DES). DES is a type of ionic solvent that can form an extended network through hydrogen bonding, allowing it to be used as a template for nanostructure growth. For example, Sun's group[40] demonstrated a method to synthesize branched Au nanostructures by reducing $HAuCl_4$ with ascorbic acid in DES at 30 °C. It is noteworthy that the DES has a triple role in the system, being a solvent, stabilizer, and liquid template. The water content in DES can be carefully controlled to modify the morphology of the Au nanocrystals, as it alters the structural features of the
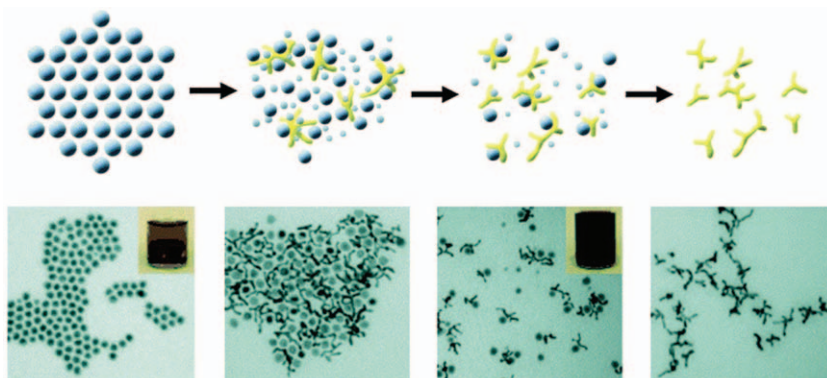
Figure 3.5   Templated growth of branched metal nanostructures. Schematic diagram of (A) functionalization of graphene oxide (GO) and the formation of the gold nanoseeds and (B) the evolution of the asymmetric 2D gold nanostructure and (C–F) the respective TEM images.
Reproduced from ref. 39 with permission from the Royal Society of Chemistry.

template. The morphology can transform from snowflake-like to star-shaped to thorny when different water levels (no water, 5000 ppm, and >10 000 ppm respectively) are present.

3.2.4   Chemical Etching

Branched nanostructures fabricated from a chemical etching approach are created through selective dissolution of certain crystallographic facets using etchants. Preparation of high yield and purity nanostructures with different morphologies is possible with careful tuning of the etchant strength. As an example, Yang *et al.*[41] were able to fabricate a series of Ag nanocrystals with different shapes using their highly selective etchant formulation. They use a 9:1 NH_4OH/H_2O_2 solution that enables etching of {100} facets over {111} facets of Ag nano-octahedra, with a high degree of selectivity. With increasing concentration of the etchant, the preferential etching in the [100] direction increases, converting the initial octahedral to octapod nanocrystals, as shown in Figure 3.6A.

The amount of branching on Pt nanocrystals can be manipulated by precise control of HCl, by oxidative etching, as demonstrated by Xiong and co-workers.[42] A mixture of H_2PtCl_6, PVP (as the stabilizer), KBr, ethylene glycol (as the reducing agent), and water were heated in air for the Pt nanocrystals preparations. With the addition of different HCl concentrations to the reaction mixture, the crystallinity of the initial Pt nanocrystals and the modes of atomic addition can be modified. The Pt nanocrystals formed initially are singly-twinned triangular nanoplates which transform into nanotripods, when HCl is not present. However, single-crystal cuboctahedral Pt nanocrystals are formed initially in the presence of HCl. These initial cuboctahedra then transform into
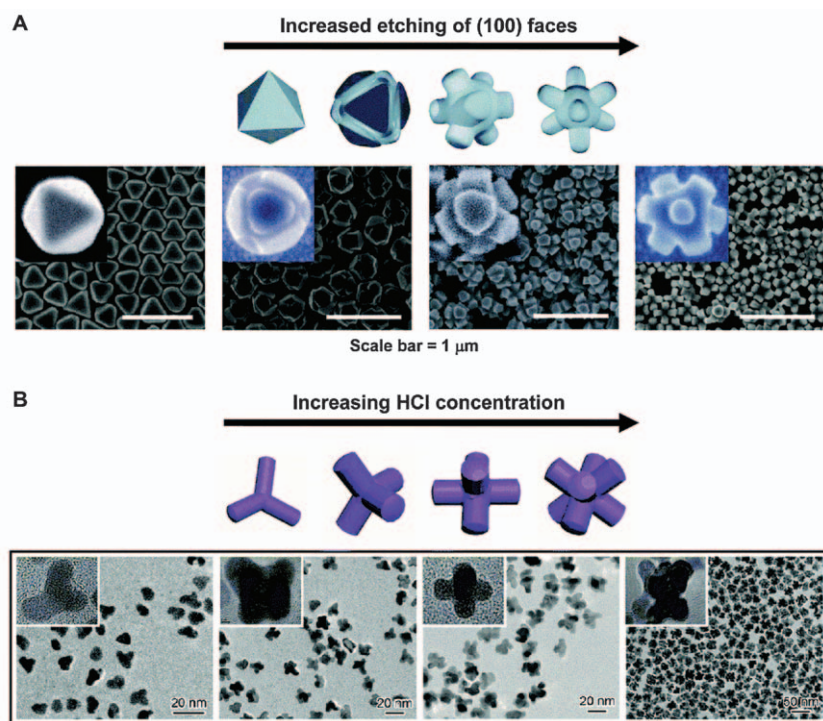
Figure 3.6 Chemical etching approach for branched metal nanostructures. (A) Schematic depiction and SEM images showing the etching progress of octahedral-shaped Ag nanocrystals using an etchant formulation that preferentially etches in the [100] direction. Reproduced from ref. 41 with permission from American Chemical Society, Copyright 2010. (B) Schematic depiction and TEM images that show the effect of varying amounts of HCl on the extent of oxidative etching of Pt nanocrystals. Reproduced from ref. 42 with permission from American Chemical Society, Copyright 2012.

multiply branched structures, with an increasing number of branches when increasing amounts of HCl are used (Figure 3.6B). This is explained as the etching strength of O_2 and Cl^- are greatly enhanced by the acidity of HCl, hence, more facets are etched oxidatively.

A unique etching process was observed by Tilley's group,[43] during the fabrication of branched Pt nanostructures in a hydrogenated atmosphere. From the study, Pt nano-octapods were obtained with the usage of a high concentration of $Pt(acac)_2$ as the metal precursor. Synchrotron-based results showed that the initial cuboctahedral nanocrystals underwent an etching process, dissolving the {100} facets and simultaneously growing along the {111} directions, to obtain the octapods. It was believed that the acetylacetonate group acts as an etchant species, as its enol form is able to etch metal surfaces *via* chelation, since traditional etchants like O_2 and halides are absent.

3.2.5   Green Synthesis

In recent years, synthesis *via* greener methods has been growing, as research is moving towards sustainability. Additionally, conventional wet-chemical synthetic methods might also use chemicals that have adverse effects on human health and the environment. Hence, prompting the research community to explore the use of biogenic materials like plant extracts, microorganisms, and biomolecules in the synthesis of branched metallic nanostructures.[44–56] Biogenic substances have their own advantages. As they are obtained from biological sources, they are considered to be environmentally benign and are biocompatible. Hence, there are suitable substitute reagents to replace toxic chemicals and ones that are considered safer to use for biomedical applications. These biogenic materials are also relatively inexpensive as compared to the chemicals used in conventional colloidal syntheses. This section will be divided into 3 subsections, which will describe how each biogenic substance is used in the synthesis of anisotropically branched nanostructures: 1) plant extracts; 2) microorganism; and 3) biomolecules.

3.2.5.1   *Plant Extracts*

In the past decade, researchers have been using a wide array of plant extracts for metal nanostructures. The phytochemicals in the plant extracts allow phytosynthesis and formation of metallic nanostructures.[44,46–48,51,54] Phytosynthesis is normally carried out in an aqueous medium under ambient conditions, which is a rapid and cheap approach that is easily scalable for bulk production. However, the exact mechanism of metal nanostructure formation *via* this kind of synthesis has not yet been fully established. Particularly, ass plant extracts have a large number of compositions, making it difficult to identify their role played in the synthesis. Nonetheless, it is generally agreeable that formation of metal nanostructures from plant extracts is a result of the synergistic action of the phytochemicals in them. Spherical nanoparticles are typically produced when phytochemicals are used.[57–61] However, in recent years, there has been an increasing number of reports on anisotropic metallic nanostructures synthesized from plant extracts.[62–74]

One of the most commonly produced branched nanostructures through a phytochemical-mediated approach is nano-flowers. For example, Thakur's group[68] used *Syzygium cumini* fruit extract to synthesize 3D flower-like Au nanostructures, with a proposed aggregation-based formation mechanism as depicted in Figure 3.7A. The two-step reaction involves a first step of phytochemical-mediated reduction of a Au precursor to obtain Au nanocrystals that are capped with the phytochemicals with conjugatable hydroxyl moieties. The nanocrystals then gradually aggregate together to form the reported multi-branched nanoflowers. Ye and co-workers[69] also reported obtaining Au nanocrystals with flower-like structures, using a similar aggregation-induced mechanism (Figure 3.7B) with star fruit juice (*Averrhoa carambola*). The fruit is rich in vitamin C and polyphenolic antioxidants,
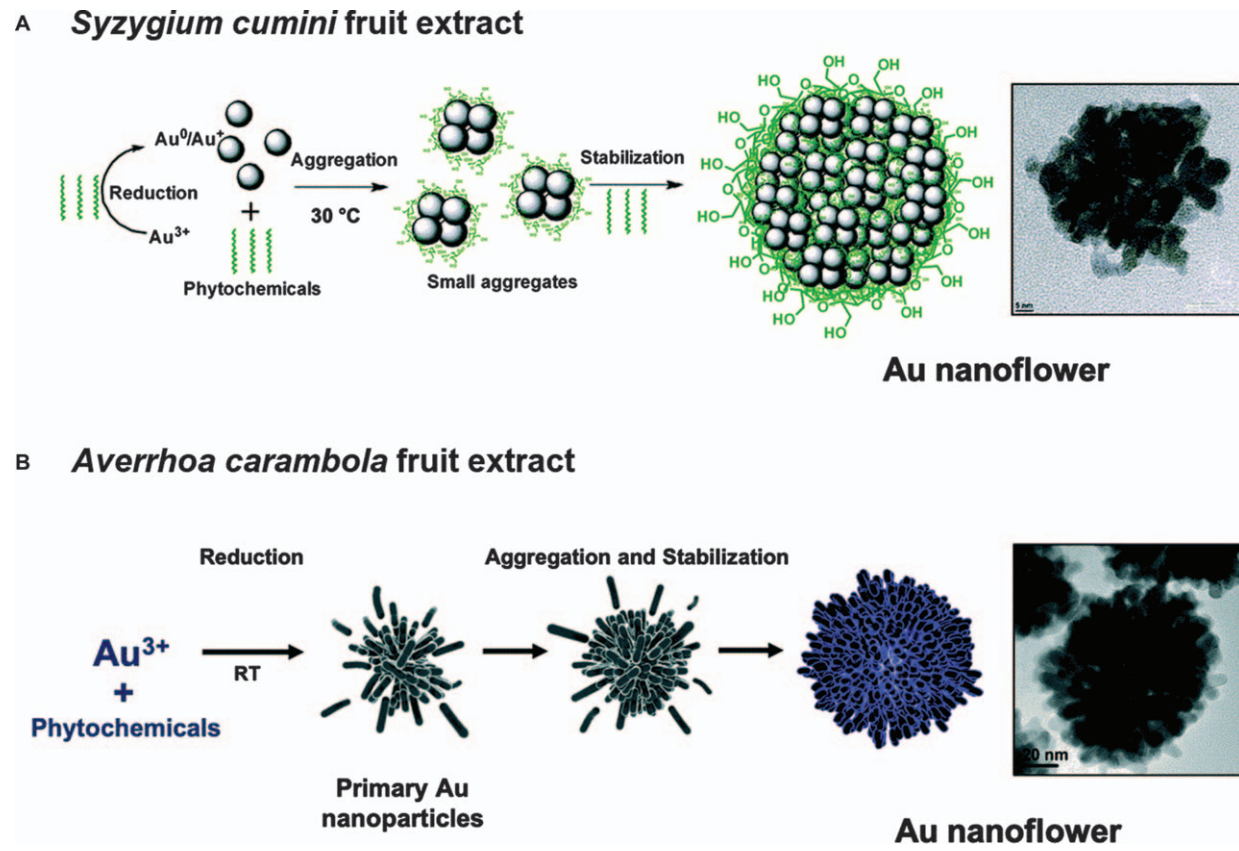
Figure 3.7 Phytochemical-mediated fabrication of nanoflowers using plant extracts. (A) Schematic illustration of the synthesis of multi-branched Au nanoflowers using *Syzygium cumini*. Reproduced from ref. 68 with permission from American Chemical Society, Copyright 2017. (B) Schematic depiction of the fabrication of Au flower-like nanostructures using *Averrhoa carambola*. Reproduced from ref. 69 with permission from the Royal Society of Chemistry.

which are good reducing and capping agents. Interestingly, Wang's group[62] was able to prepare a variety of 3D multi-branched Au nanocrystals (*e.g.* flower, urchin, and confeito structures) through reduction of an Au precursor with gum arabic. The hydroxyproline-rich gum arabic acts as a capping agent, which is critical to the growth of nanostructures through a successive aggregation model.

Bimetallic flower-like nanostructures are also reported by using plant extracts. For instance, Sun *et al.*[64] reported the formation of such a material with an Au core and Pd petals through a seeded growth approach that involves successive reduction of the Au and Pd precursors and room temperature. The Au precursor was first reduced using ascorbic acid to form Au seeds. The Pd precursor was then added gradually, followed by the introduction of *Cacumen platyclade* leaf extract. The Au seeds formed acted as nucleation points for the aggregation and growth of Pd petals, obtaining the Au–Pd core–petal nanoflowers. The gradual introduction of the Pd precursor and usage of plant extract as a mild reductant and capping agent are essential for controlling the nucleation rates of Pd. These ensured that the Pd are deposited on the Au seeds and not forming separate Pd nanostructures. The low temperature used also prohibited interdiffusion of atoms between the Au core and Pd petals. Intriguingly, alloyed AuPd nanoflowers were obtained instead of a core–petal structure when reduction of Au and Pd precursors occur simultaneously.[65]

3.2.5.2   Microorganism

As microorganisms (bacteria and fungi) have the ability to detoxify heavy metals, they have sparked substantial interest in applications in metal nanostructure synthesis *via* a biomimetic approach.[75,76] They have metal-binding proteins that are efficient in reducing metal ions through both intracellular and extracellular reduction mechanisms. Additionally, metal nanostructures can grow into intricate morphologies as the surface structure of microorganisms can serve as an excellent templating medium.[77–79]

Li and co-workers[66] reported using *Escherichia coli* bacteria to synthesize dendritic and horn-like Au nanostructures. In the presence of cationic surfactant, the Au ions are first biosorbed and reduced by the microbial surface, forming tiny Au nanoparticle nuclei. Ascorbic acid was added to enhance the reduction process as the microbial reduction was slow even when the biosorption happens readily. The Au nanoparticle nuclei linked themselves together through linear fusion and grew progressively on the microbial surface, forming dendritic Au nanostructures. The dendritic nanostructures then eventually grow into nanofilms as the Au nanoparticles filled the gap in between the branches. Ultimately, the two Au nanofilms formed between the adjacent bacterial cells merge and form a unique horn-like morphology, which is rarely seen *via* traditional wet-chemical synthesis. Au nanohorns were also synthesized *via* a similar microorganisim-mediated mechanism, using yeast *Pichia pastoris*.[80]

Pd and Pt nanoflower fabrication with the use of fungal mycelia of *Rhizopus oryzae* was reported without additional reducing agent.[81] The cell surface proteins of the mycelia have various functionalities which allow the fungi to serve several roles (reducing, capping, and shape-directing agents) during the fabrication. A similar Pd nanoflower structure was also obtained using *Pichia pastoris*, but with ascorbic acid present.[82] *Pichia pastoris* is also capable of being utilized for the fabrication of alloyed AuPd nanoflowers with H_2 as the reductant (Figure 3.8).[83] The Au ions reduce on the cell surface, followed by a reduction of Pd ions, which aggregate on the Au surfaces. This sequence leads to a flower-like nanostructure with an Au core and Pd petals initially. However, due to the interdiffusion process, homogeneously alloyed AuPd nanoflowers are obtained.

3.2.5.3   Biomolecules

Biomolecules can be broadly termed as molecules that are present in organisms that are typically essential to biological processes. They can be of large molecules such as proteins, carbohydrates, lipids, and nucleic acids, or small molecules like vitamins and other metabolites.

The most commonly used biomolecule for synthesis of metallic nanocrystals is vitamin C (or ascorbic acid). Vitamin C is not only a potent antioxidant (reducing agent), but is also non-toxic and biocompatible, making it a superior candidate for synthesis of nanostructures with biological applications. Typically, ascorbic acid acts exclusively as the reducing agent and does not participate in morphological control. For example, both Vo's[84] and Lv's[85] teams used ascorbic acid as a reducing agent in a one-pot synthesis of branched Au nanoparticles. However, some studies suggest that ascorbic acid is able to do morphological directing. For instance, Wang and co-workers[86] reported the synthesis of hyperbranched Pt nanostructures using only Pt precursors (K_2PtCl_4) and ascorbic acid. The resultant branched morphology of the Pt nanocrystals was attributed to 2,3-diketo-1-gulonic acid (DGA), which is an oxidation by-product of ascorbic acid. As shown in Figure 3.9A, ascorbic acid undergoes an oxidation process and forms dehydroascorbic acid (DHA). However, DHA is not stable and converts to DGA spontaneously through hydrolysis of the lactone ring. The DGA molecules can selectively bind to specific facets of the growing Pt nanocrystals through their carboxyl functionality. The theoretical calculations supported the proposed mechanism, which revealed the preferential binding of DGA onto Pt (100) and (110) facets. As a result, the growth in these two directions was restricted and only growth of Pt (111) was observed, and anisotropically branched Pt nanostructures are formed. Yang's group[87] also reported a similar method for their Au nanourchin growth, using only Au precursor and ascorbic acid. The schematic diagram of the proposed mechanism is shown in Figure 3.9B. Nanoflowers with an Au core and Pt petals were also reported by addition of ascorbic acid and Pt precursor into a boiling solution of pre-formed Au seeds.[88]

Another class of biomolecules that are used frequently is deoxyribonucleic acid (DNA). Due to its well-defined and sequence-specific structure, it is
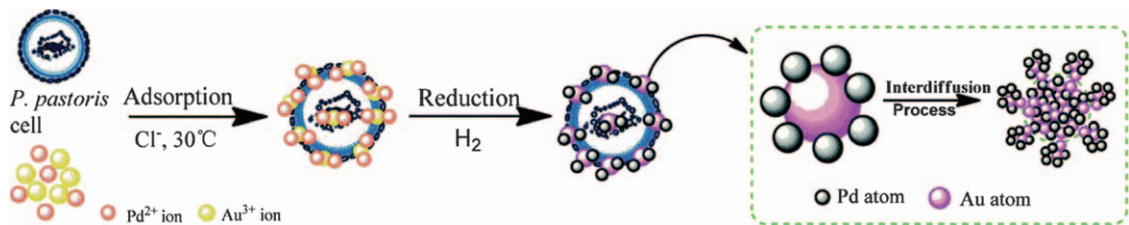
Figure 3.8 Microorganism-assisted formation. Schematic illustration of the fabrication of AuPd nanoflowers using *Pichia pastoris*. Reproduced from ref. 83 with permission from the Royal Society of Chemistry.
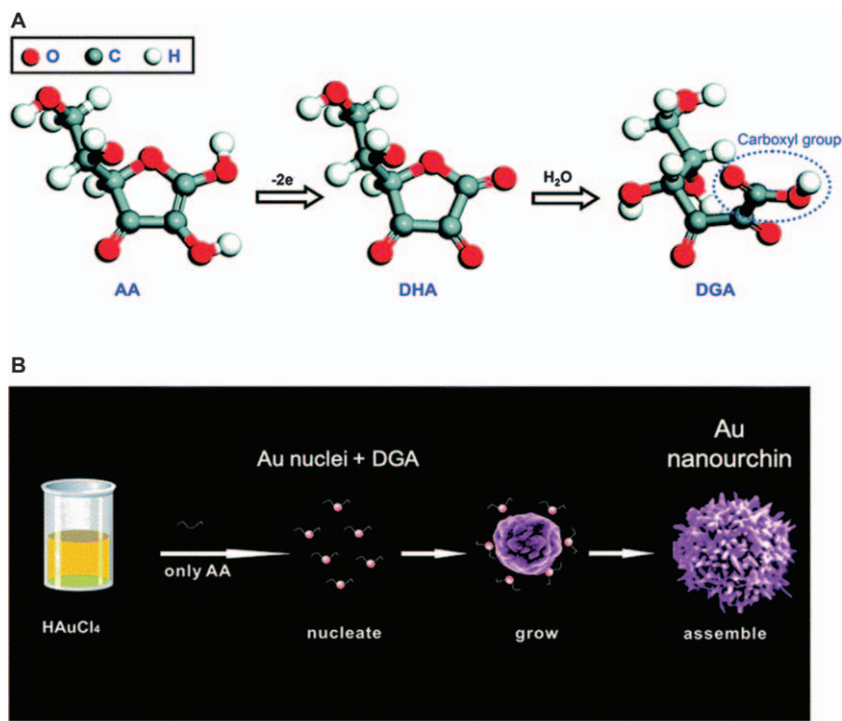
Figure 3.9 (A) Synthetic scheme of ascorbic acid (AA) to 2,3-diketo-1-gulonic acid (DGA). Firstly oxidation of AA to dehydroascorbic acid (DHA), followed by hydrolysis to DGA. Reproduced from ref. 86 with permission from American Chemical Society, Copyright 2010. (B) Schematic representation of the DGA-mediated growth of Au nanourchins. Reproduced from ref. 87 with permission from the Royal Society of Chemistry.

usually used to provide a skeletal framework for template directing synthesis of metal nanostructures with unique morphology. For instance, Song *et al.*[89] reported synthesizing X- and Y-shaped Au nanocrystals using similarly shaped DNA templates (Figure 3.10A). Single-stranded oligonucleotides, that are half-block complementary to each other, were annealed together to form the DNA templates. Either a four-armed DNA (X-DNA) or a Y-armed DNA (Y-DNA) were obtained from the hybridization of four or three strands of oligonucleotides, respectively. When Au precursor was added, complexation of the Au ions with the DNA templates occurred. The bound Au ions were then reduced and X- and Y-shaped Au nanostructures were formed.

Lu's group[90] examined the effect of three types of single-stranded 30-mer DNAs comprised of poly A, poly C, and poly T (A30, C30 and T30) on the growth of Au nanocrystals from pre-synthesized nanospheres. A30 and C30 have a much higher binding affinity to Au nanospheres which promotes inhomogeneous growth and Au nanoflowers are obtained. On the other hand, T30 has a lower binding affinity with the Au nanospheres, hence, is not able to induce growth of
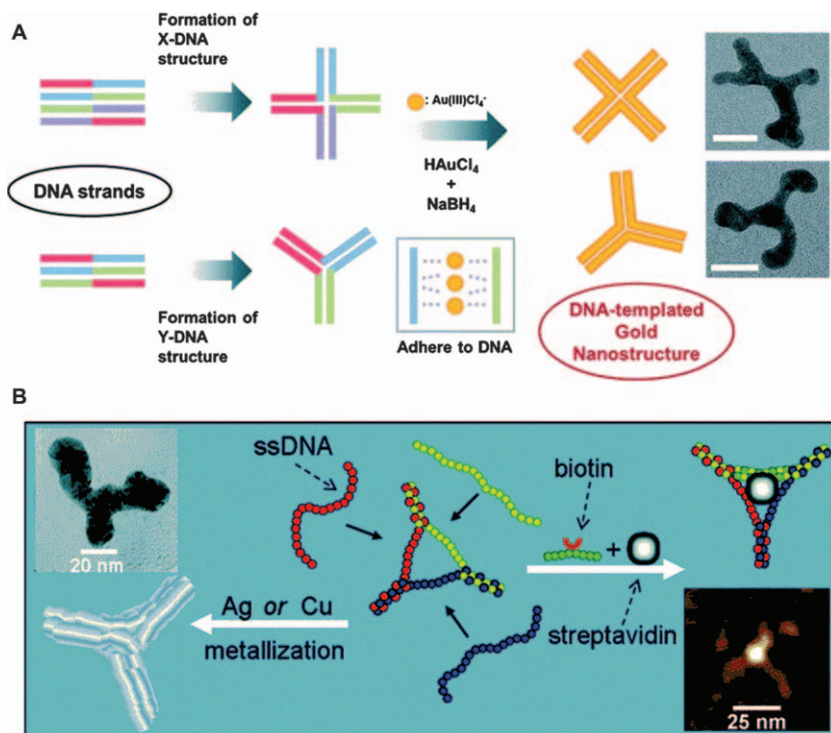
Figure 3.10 Branched nanostructure synthesis using DNA as a template. (A) Schematic depiction of the DNA-templated synthesis of four-armed (X-shaped) and three-armed (Y-shaped) Au nanostructures. The TEM images of the final branched structures are also shown (scale bar: 20 nm). Reproduced from ref. 89 with permission from the Royal Society of Chemistry. (B) Schematic depiction of the formation of branched Ag and Cu nanostructures using a branched template based on DNA–protein assemblies. Reproduced from ref. 92 with permission from American Chemical Society, Copyright 2005.

anisotropic nanostructures, resulting in only bigger nanospheres. In a subsequent study, they investigated the effect of different DNA sequences on the growth of Au nanostructures using pre-synthesized Au nanoprisms.[91] The Au nanoprisms used were planar twinned crystals with {111} facets on both the top and bottom surfaces, with stacking faults at the side faces. The resulting Au nanocrystals have varying morphologies, including multi-tipped nanoflowers and six-tipped nanostars, as the DNA sequences bind differently to the exposed facets of the nanoprisms, leading to the growth of the seeds in different directions. Branched Ag and Cu nanostructures were synthesized using DNA–protein assemblies as templates (Figure 3.10B).[92,93] The DNA–protein template has a streptavidin protein core that is conjugated to a biotinylated DNA molecule. Metallization of the template results in branched metal nanostructures forming, and the lengths of the branches can be controlled by the size of DNA. Meanwhile, Huang and co-workers used the nucleotide guanosine
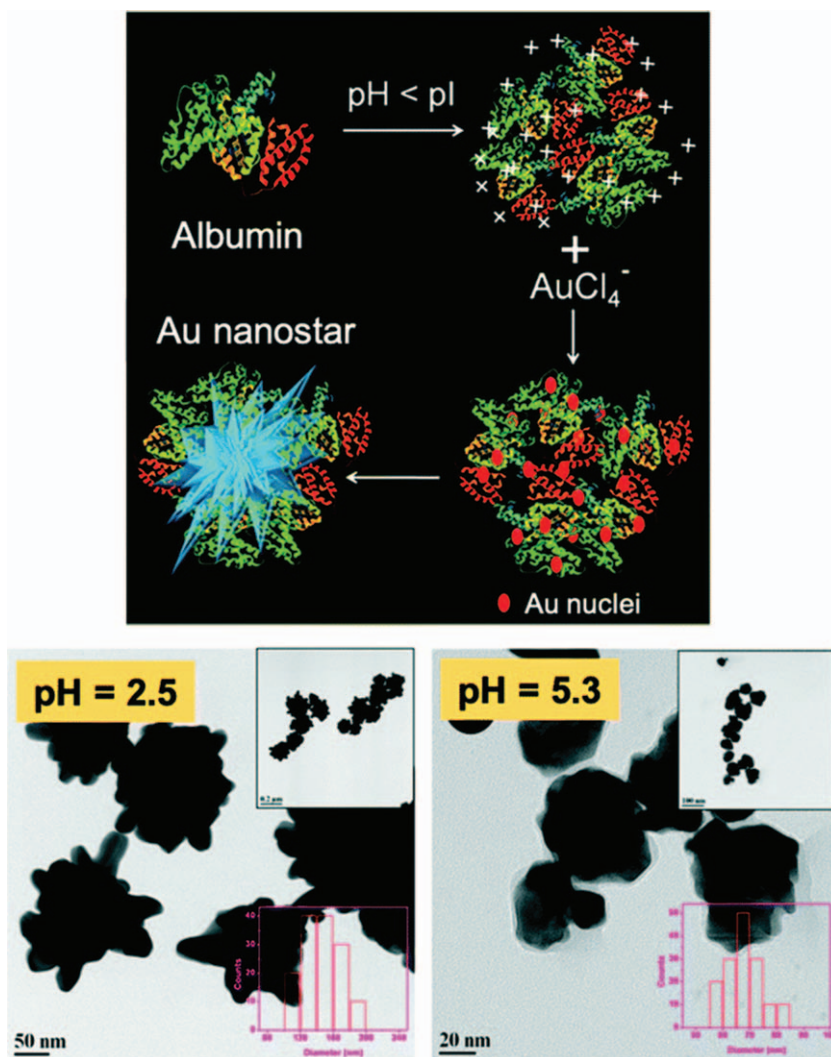
Figure 3.11 Schematic illustration of the albumin-directed synthesis of multi-tipped Au nanostars. The formation of a nanostar is promoted when the solution pH is less than the isoelectric point (pI) of albumin, which is 4.7 (for bovine serum albumin).
Reproduced from ref. 95 with permission from American Chemical Society, Copyright 2017.

5′-monophosphate (5′-GMP) as the capping agent to control the synthesis and Au nanoflowers with abundant tips are obtained.[94]

Just like DNA, protein is also a good candidate as a template for directing the shape of metal nanostructures. For example, Srivastava *et al.*[95] reported the use of albumin as a template for the fabrication of multi-tipped Au nanostars, as shown in Figure 3.11. To generate the star-shaped morphology, the pH of the

reaction mixture plays a critical role. pH values lower than the isoelectric point
(pI) of albumin are especially favored as the net positive charge will allow the
attachment of the Au precursor ions $(AuCl_4^-)$ to it. Additionally, at such a low
pH value, the α helices in albumin are stretched in such a way that they
transform into β sheets, hence easing the access to attach the Au precursor to
the functional groups. The β sheet conformation also allows the reduced Au
nuclei to be readily evolved to the spiked nanostars. In a separate study, the
same group uses poly(L-arginine)-albumin core–shell nanoparticles as seeds to
prepare albumin-stabilized Au nanostars.[96] And on a separate paper, albumin
is used primarily as a stabilizing agent.[97] The as-synthesized Au nanostars
had inherit stability, functionality, and biocompatibility due to albumin's
non-toxicity and binding capabilities. As a result, these albumin-stabilized Au
nanostars showed compatibility toward cells and human blood.

Anisotropically branched metal nanostructures can also be synthesized
through enzymatic synthesis pathways. Li's group[98] demonstrated the fabri-
cation of Au nanoflowers through such a pathway using trypsin, which is a
proteolytic enzyme that is present in the human digestive system. Similar to
albumin, the attachment of $AuCl_4^-$ to trypsin is favorable when the reaction
mixture has a lower pH than trypsin's pI. These $AuCl_4^-$ ions that are bound
to trypsin were then reduced by ascorbic acid to form Au nanoparticles.
The cysteine residues in trypsin have thiol functional groups which readily
bind to the different crystallographical facets on the Au nanoparticles,
resulting in anisotropic growth into nanoflowers. Ma *et al.*[99] reported the
synthesis of Ag nanoflowers with the use of only the amino acid L-cysteine and
$AgNO_3$. L-cysteine is believed to have a triple role of reducing, capping, and
shape-directing capabilities.

Carbohydrates can also be employed in the synthesis of anisotropic metal
nanocrystals. For instance, Nhung and co-worker used chitosan to mediate the
synthesis of both Au[100] and Ag[101] nanoflowers. A schematic of the chitosan-
mediated growth process is shown in Figure 3.12A. The process involves
mixing of the metal precursor with ascorbic acid (as a reductant) and 50 kDa
chitosan (as a template). Chitosan has amino and hydroxyl moieties that can
bind to specific facets of the nucleated metal nanocrystals, leading to selective
facet growth. Additionally, its flexible molecular conformation enables
adjacent chains to trigger aggregation of the nucleated metal nanocrystals and
support the growth into Au nanostructures with hierarchical flower-like
morphology. Carrageenan, a liner sulfated polysaccharide present in some
seaweeds, is utilized for the preparation of Pd nanoflowers with thorn-like
petals.[102] As shown in Figure 3.12B, the Pd precursor was reduced using as-
corbic acid, in the presence of carrageenan (as a capping agent). Carrageenan
has hydroxyl and sulfate functional groups which can interact with specific
facets of the growing nuclei, directing them to form Pd nanoflowers.

Monosaccharides like fructose are also reported being utilized in a hydro-
thermal process to obtain dendritic Pt nanostructures.[103] The hydrothermal
reaction was performed at 180 °C, in which a thermolytic reduction had oc-
curred. It has been hypothesized that fructose not only serves as a reductant,
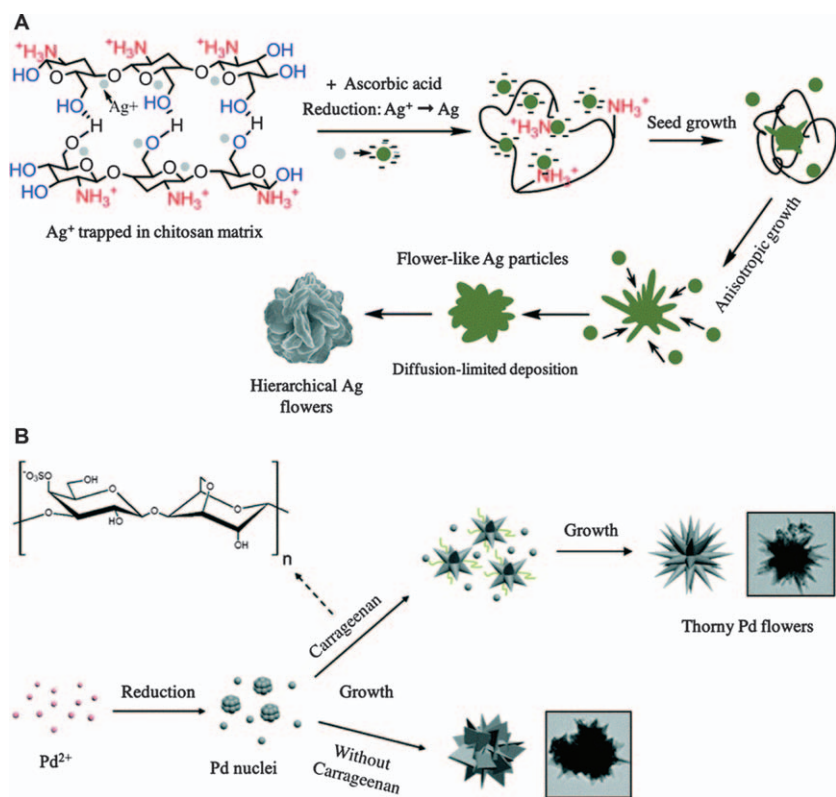
Figure 3.12 Formation of anisotropic metal nanostructures using carbohydrates as shape-directing agents. (A) Schematic depiction of chitosan-directed formation of hierarchical flower-like Ag architectures. Reproduced from ref. 100 with permission from American Chemical Society, Copyright 2014. (B) Schematic illustration of the carrageenan-assisted formation of thorny flower-like Pd structures. Reproduced from ref. 102 with permission from American Chemical Society, Copyright 2018.

but also acts as a source of hydrothermal carbon (HTC). HTC can bind onto the Pt surface and promote anisotropic growth into dendritic structures.

3.3 Optical and Photothermal Properties

Metallic nanostructures of varying morphologies have been vastly employed in an array of applications today for their optical properties. When certain metals are diminished to a size smaller than the wavelength of light, the light–metal interactions occurring can lead to a phenomenon known as the localized surface plasmon resonance (LSPR) effect. LSPR is commonly observed in noble metals such as gold and silver, and to a smaller extent in other non-noble metals such as aluminum and palladium. Notably, the LSPR absorption bands of Au and Ag lie in the visible region. Alongside other favorable properties such as chemical stability, good biocompatibility, and ease of surface

functionalization, they can be employed in various advanced applications   1
such as sensing,[104,105] alternative medical treatment, and photocatalysis.[106]
For this reason, the bulk of this chapter will be based on Au nanostructures.

When these metallic nanoparticles (NP) are irradiated with light, the sur-
face electrons will be excited and cause a polarization of charges between the   5
metal surface and the nuclei. This is counteracted with a coulombic restoring
force that consequently affects the oscillation of these conduction band
electrons, commonly termed as surface plasmon.[107] However, when this
oscillation frequency coincides with the frequency of light that is irradiated,
the absorption of (resonant) incident light produces intense and localized   10
electric fields in its immediate surrounding, giving rise to the LSPR effect.

As LSPR activities are conducted at the surface, it is highly susceptible to
changes in the morphology of the metallic NPs and/or its contagious
medium.[107] The LSPR absorption band (and therefore its optical properties)
of the metallic NPs can thus easily be tuned by altering its size or shape. The   15
variation in sizes of metallic NPs can be a very simple approach to modulate
its optical properties, but a variation in shape offers more versatility in many
situations due to the prospect of having different physiochemical properties
at different facets of the nanostructure. This has spurred material chemists
to innovate distinctive anisotropically branched nanocomposites with   20
unique and complex configurations:[108] nanocrosses,[109] nanoflowers, and
nanohexapods, to name but a few. These nanostructures are designed and
verified to be excellent light absorbers and scatterers due to enhancements
that are brought about by their structural features.

After the absorption of light by the metallic nanostructures, the excited   25
electrons would tend to liberate the additional energy they come to possess
through a couple of relaxation pathways. One possible outcome of such
relaxation is localized heating of metallic nanostructures. Upon the photo-
excitation of conduction electrons, non-thermal hot carriers that are gener-
ated *via* Landau damping proceed to disseminate their energy through   30
electron–electron scattering, resulting in internal electron thermalization.[110]
Following this is the diffusion of thermal energy to its vicinity (*i.e.* the pho-
tothermal effect), while the metallic nanostructure cools down and stabilizes.

The inclusion of branched features in a metallic nanostructure's morph-
ology can be remarkably beneficial as they can strengthen the photothermal   35
effect. With the existence of branches, plasmonic hot spots can be established
where the electromagnetic fields would be intensely magnified in small
pockets of space (*i.e.* the tips of the branches). These hot spots are quint-
essential in producing increased hot carriers from the disruption of linear
momentum of the electron in the hotspots[111] and hence an amplification in   40
the photothermal effect. When a considerable amount of heat can be gener-
ated in its locality, the photothermal effect can be effectively exploited for
practical applications,[105] notably in minimal invasive cancer treatments such
as photothermal therapy and photothermal-induced chemotherapy. In the
following sub-sections, selected branched metallic nanostructures that make   45
excellent photothermal transducers are showcased and elaborated on.

3.3.1 Nanoflowers, Nano-urchins, and Nanodendrites

Ideally, a good photothermal transducing agent should not only absorb light proficiently in the NIR region but also maintain appropriate sizes for therapeutic applications. This cannot be achieved with just Au NPs as their LSPR absorbance lie in the visible region and they absorb poorly in the NIR region. Hupp *et al.*[112] and Gao *et al.*[113] reported a red shift in SPR absorption bands when branched features were introduced to Au NPs. Hence, branched variants of the Au NPs, such as nanoflowers, nano-urchins and nanodendrites can be attractive candidates in the making of a good photothermal transducer. In an instance, the optical and photothermal properties of Au nanoflowers have been explored by Ye and co-workers[69] (Figure 3.13). By simply adding an Au precursor ($AuCl_3$) to star fruit juice, Au nanoflowers (GNFs) of average diameters ~100 nm were synthesized (Figure 3.13B). Next, the absorption spectrum
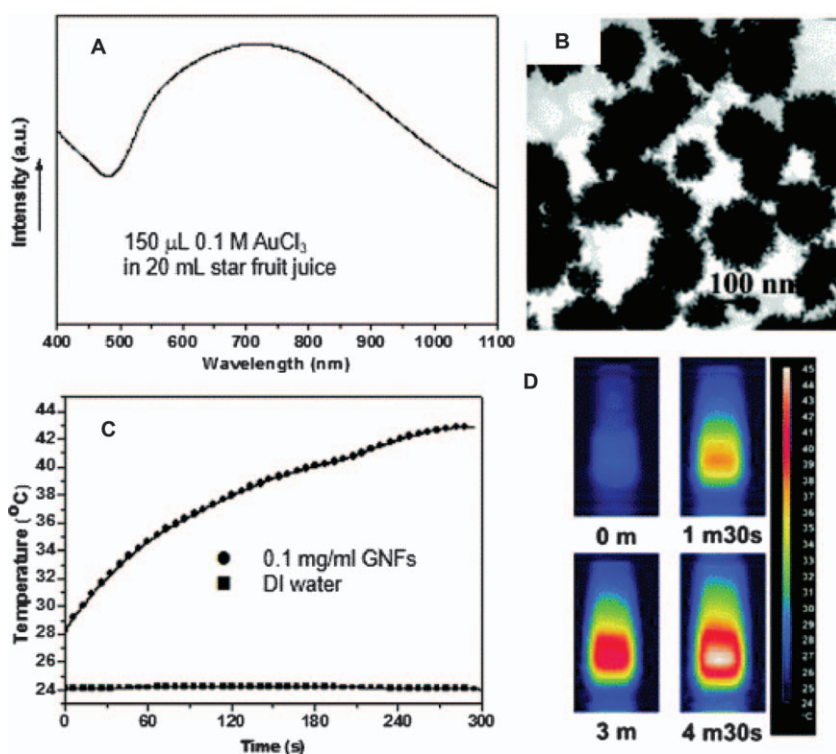
Figure 3.13 Characterization of GNFs for their optical and photothermal properties: (A) Absorption spectrum of GNFs after the reaction of a gold precursor in star fruit juice; (B) corresponding TEM image of the GNFs; (C) temperature elevation of water by GNFs upon irradiation with an 808 nm laser with a power density of $1 \ W \ cm^{-2}$; (D) Corresponding thermographic images recorded at different time intervals.

of the GNFs was obtained and a broad absorption peak that spans from 500 nm
to 1100 nm is observed in Figure 3.13A, peaking at around 725 nm. This is in
contrast with typical Au nanospheres which have an absorption peak at
~570 nm and absorb poorly in the NIR region. With an establishment of its
absorption spectrum, the GNFs were further subjected to a simple setup where
they were shorn with an 808 nm NIR laser with a power density of 1 W cm^{-2} to
evaluate their suitability as photothermal agents for therapeutic purposes.
By measuring the temperature of the aqueous medium with an infrared
camera, it can be seen that there is a significant increase in temperature
(~14 °C) when compared to a control setup of pure water (Figure 3.13C and D).
This underscores the GNFs ability to act as a photothermal transducer upon
absorption of NIR light and release heat to its locality.

The photothermal stability of GNFs was additionally conducted by Wang
et al.[114] and Gao *et al.*[115] In Wang and co-workers' study, the irradiation of a
785 nm laser with 1.5 W cm^{-2} power for 10 min resulted in a 10 °C increase in
its aqueous medium (3 °C for pure water). After 5 cycles of recurred heating, the
GNFs did not experience any change in their morphology. Conjugates of the
GNF were also verified to be stable after 30 min of laser irradiation. The results
were mirrored in Gao and co-workers' study where their conjugated GNFs were
able to achieve rapid thermalization under 2 min of 808 nm laser irradiation.
After 30 min of laser irradiation, the conjugated GNFs remained stable, as its
spectral profile, hydrodynamic size, and morphology remained almost un-
perturbed. Hence, from the mentioned studies, GNFs exhibit desirable optical
and photothermal properties for photothermal transducing applications.

In the same vein, Au nano-urchins (GNU)[116–118] and Au nanodendrites
(GND) have multiple branches like GNFs that enable tuning of their LSPR
absorption bands for effective photothermal applicability (Figure 3.14 and
3.15). For example, Djaker *et al.*[116] experimented with the irradiation of
808 nm laser on Au NPs and GNUs and reported an increase in temperature
elevation speed in water of about 80% when GNU was compared with Au NPs
(Figure 3.14C and D). They attributed this finding to the closer proximity of
GNU's LSPR absorption peak to the laser irradiation and a greater absorption
cross-section (σ_{abs}). Based on experimental results and the Mie theory, the
growth in σ_{abs} was estimated to be in the range of 60–80%. Meanwhile,
Ong and co-workers demonstrated tunability in controlling the morphology
of their Au nanostructure between GNF and GNU *via* Ag^{+} which acted as a
shape-directing agent.[117] In this, they were able to fabricate GNUs were
"pointier spikes" that were accompanied with a red shift in LSPR absorption
from the visible to the NIR region. The GNUs were also robust when tested for
their photothermal effect and any changes in their structural integrity after
808 nm laser irradiation.

On the topic of GNDs, the studies of Wang *et al.*[119] and Mao *et al.*[120] have
demonstrated the complexity in tuning the absorbance spectrum of GNDs
where it is influenced by various factors such as aspect ratio, inter-branching
gaps, dendritic length, and density, *etc.* Both studies reported a red shift of
LSPR absorption bands with increases in dendritic length. This is analogous
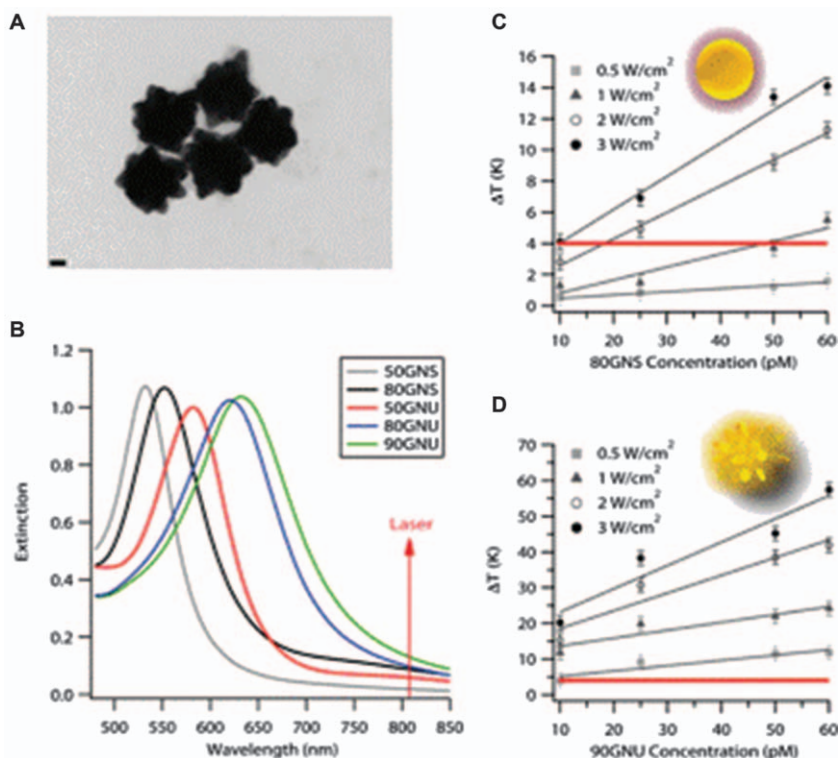
Figure 3.14 Characterization of Au nanourchins (GNU) for their optical and photo-thermal properties: (A) TEM images of the GNUs; (B) absorption spectra of Au nanospheres (GNS) and GNUs of different sizes; (C and D) temperature elevation of water by GNS and GNU after 15 min of irradiation with an 808 nm laser at different power densities.
Reproduced from ref. 116 with permission from American Chemical Society, Copyright 2019.

to the concept of red shifting the absorption band of a nanorod by extending its length. However, a difference in results was observed with regard to altering the dendritic density. In Wang and co-workers' study, the increase in dendritic density resulted in slight increases in the GND's size and brought about a red-shift in its absorption band to 1064 nm as compared to GNDs of lower densities or Au NPs (Figure 3.15A and B). On the other hand, in Mao and co-workers' study, the increase in dendritic density resulted in a blue shift in the absorption maxima to about 700 nm with poorer extinction coefficients at longer wavelengths. It was elucidated that the increase in dendritic density was compensated with shorter dendritic length, resulting in the sparser GND having a red-shifted absorption peak compared with the denser ones. Hence, the mentioned references showcase the utility of branched elements in tuning the optical profile of Au nanostructures for photothermal applications.
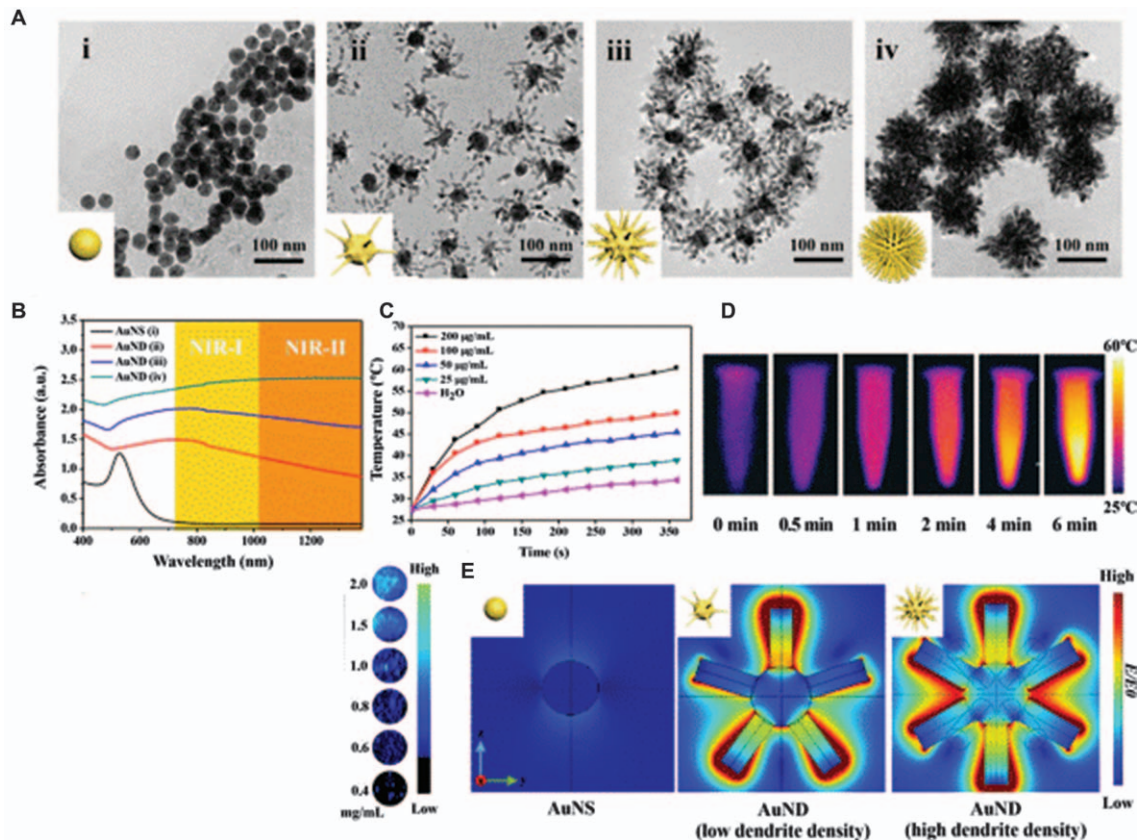
Figure 3.15 Characterization of Au nanodendrites (GND) for their optical and photothermal properties: (A) TEM images of the Au nanoseed (i) and GNDs with different branch densities (ii–iv); (B) absorption spectra of GNDs with different branch densities; (C) temperature elevation curve of water by GNDs under 1064 nm laser irradiation with a power density of 1.0 W cm^{-2} for 360 s); (D) representative photothermal images of GND solution (100 µg mL^{-1}) under 1064 nm laser irradiation with power density of 1.0 W cm^{-2} at various irradiation time points; (E) COMSOL simulation with a 785 nm laser irradiation which illustrates the hotspots of the GND at the dendritic tips.
Reproduced from ref. 119 with permission from American Chemical Society, Copyright 2021.

3.3.2 Nanocrosses

Besides Au NPs, the nanorod is another morphology that is ubiquitously utilized for photothermal applications.[121–124] While nanorods can achieve NIR absorption at large aspect ratios, the introduction of branched features can conceivably give rise to augmented capabilities. The nanocross is one such adaptation that possesses a cross-like morphology extending in transverse and longitudinal directions, unlike nanorods which only extend in one direction. The plasmonic properties of Au nanocrosses have been investigated by Han *et al.*[109] Figure 3.16A exhibits the TEM images of their fabricated Au nanocrosses, and it can be discerned that the Au nanocrosses are shaped by two longer branches along the ⟨110⟩ direction and two shorter ones along the ⟨001⟩ direction. In its absorption spectrum (Figure 3.16B), two distinct signals were observed – a gentler peak in the visible region at around 550 nm and an intense but broad absorption band enveloping over the NIR region (*i.e.* 800 nm to 1200 nm). The two signals are ascribed to the transverse and longitudinal branches, respectively. By altering the growth conditions of the Au nanocrosses, *i.e.* time for growth of the crystal and use of different reducing agents, the absorption peaks in the spectrum could be tuned accordingly.[26,125] For instance, a shift in absorption peak toward shorter wavelengths was seen when smaller Au nanocrosses were fabricated.

Further investigations on the influence of shape on the optical properties of nanocrosses were performed using monochromated electron energy-loss spectroscopy (EELS).[126] Figure 3.16C illustrates the scanning TEM (STEM) dark field image of a sample Au nanocross, overlaid with monochromated energy filtered TEM (EFTEM) maps of the plasmonic modes in the nanocross. In addition, a 1 mm electron probe was placed at the five locations of the right image in Figure 3.16D to give the corresponding monochromated EELS spectra in Figure 3.16D. It was revealed that there exist three main plasmonic modes in the nanocross, represented in Figure 3.16C, and that radiation damping is prevalent at NIR energy ranges below 1.6 eV where the aspect ratios are large. The enumerated spectra of the plasmonic modes in Figure 3.16D reiterate the pronounced NIR absorption of the nanocross. Discrete dipole approximation studies were also conducted to probe the synergistic coupling of the four branches in the Au nanocross.[109] It was discerned that any of the branches could act as reception points for the excitation of the entire nanocross. The proficient absorption of NIR light and ability to activate the entire nanocross at any "receptor" branches allow the nanocrosses to serve as bi-directional nanoantennas that can efficaciously harvest incident light for succeeding purposes, *i.e.* photothermal transduction.

3.3.3 Nanohexapods

The general favorability toward multiple branched configurations can be understood due to plasmonic modes occurring at the tips of the branches.[107]
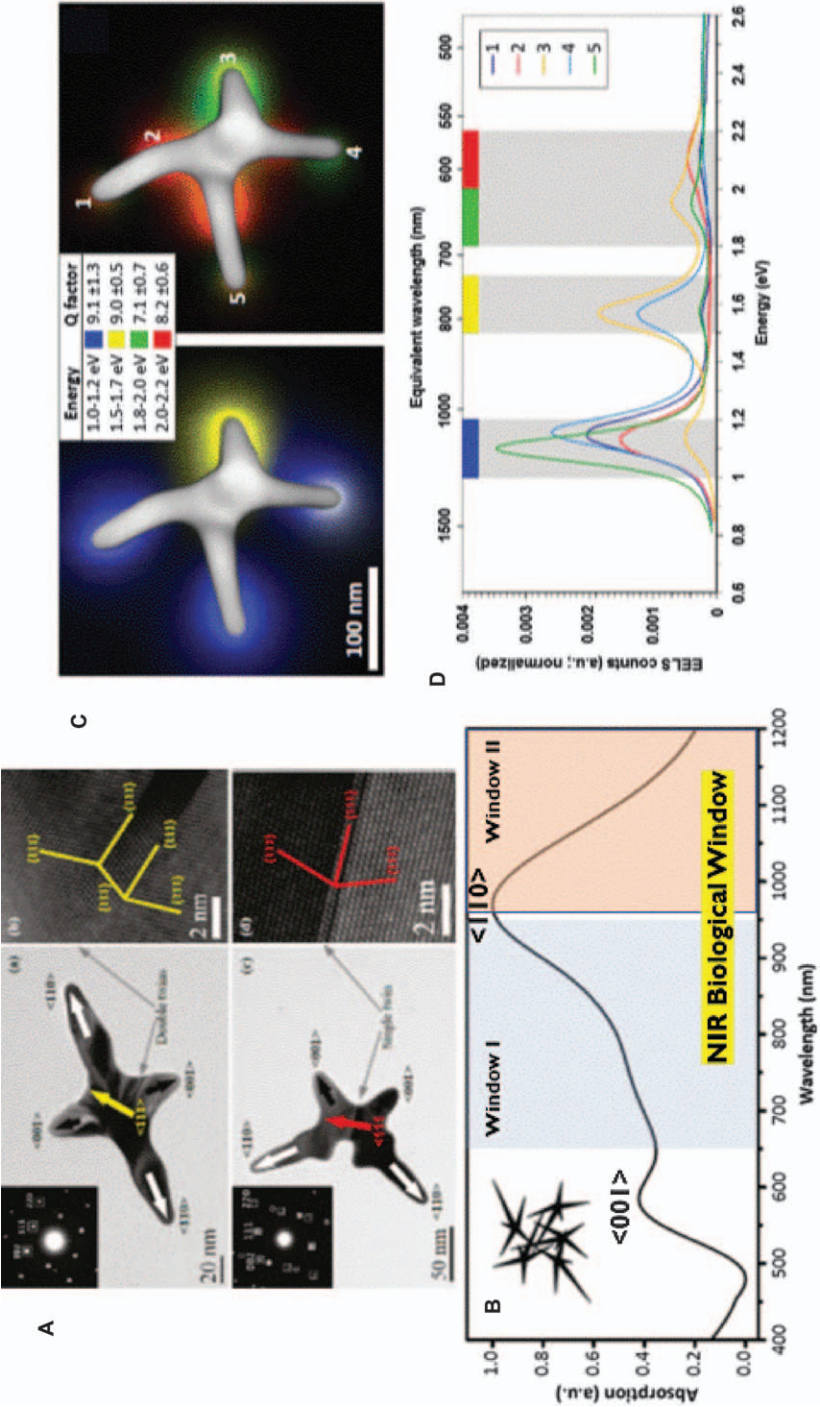
However, many of these nanostructures possess an arbitrary number of arms with a span of differing arm lengths. Specificity in shape design could be desirable in enabling us to control the optical properties of the nanostructure at will. In this aspect, Xia *et al.* fabricated Au nanostructures with six designated arms – Au nano-hexapods (GNH).[17,127] The arm length and correspondingly the spectral profile of these GNHs can be tuned by adjusting the concentration of Au precursor ($HAuCl_4$) and reaction temperature. When the GNH is pitted against Au nanorods and nanocages of similar spectral profiles (Figure 3.17), a relatively similar photothermal effect was observed among the three nanostructures. However, the GNHs and nanocages had better photothermal stability than the nanorods, where exposure to an 805 nm laser at a power density of 15 mW cm^{-2} for 15 min melted the nanorods but not the GNHs and nanocages. In addition, DDA studies identified several plasmonic peaks between 700 and 900 nm which correspond to GNH in various orientations.

3.3.4 Other Branched Metallic Nanostructures with Strong NIR Absorption

Besides the above nanostructures, there exist a diverse range of anisotropically branched nanostructures with strong NIR absorption that could potentially be used for photothermal applications. For example, Au bellflowers (GBF) were synthesized by Chen *et al.* using a liquid–liquid–gas triphase interface system.[128] The GBFs have a unique morphology which consist of a V shape dome for intensification of acoustic signals while there are also numerous branched petals for strong NIR absorption and photothermal effect (photothermal efficiency, η ~74%). Au nanostars[129–133] have also been prevalently studied for photothermal transducing purposes, attributed to their strong LSPR absorbance band in the NIR region (Figure 3.18B).

Figure 3.16   Characterization of Au nanocrosses. (A) TEM images showing the Au nanocrosses existing as (top) double twin and (bottom) single twin. Reproduced from ref. 109 with permission from American Chemical Society, Copyright 2011. (B) Vis–NIR absorption spectra of the Au nanocrosses, where there is a strong absorption peak in the NIR region. Reproduced from ref. 125 with permission from John Wiley and Sons, Copyright © 2016 WILEY-VCH Verlag GmbH & Co. KGaA, Weinheim. (C) Visualization of plasmonic modes using monochromated EELS maps where (left) maps the modes at 1.1 eV and 1.6 eV and (right) maps the modes at 1.9 eV and 2.1 eV; (C) monochromated EELS taken in STEM mode, by placing a 1 nm electron probe at locations 1–5 indicated in the panel (C, right). All five spectra were normalized at the 'zero-loss peak' maximum, after which a pre-measured background was subtracted. The spectral peaks represent the plasmon modes, around which the color-coded, gray 0.2 eV energy windows were placed for the EFTEM experiments, giving the maps in (C). Reproduced from ref. 26 with permission from the Royal Society of Chemistry.
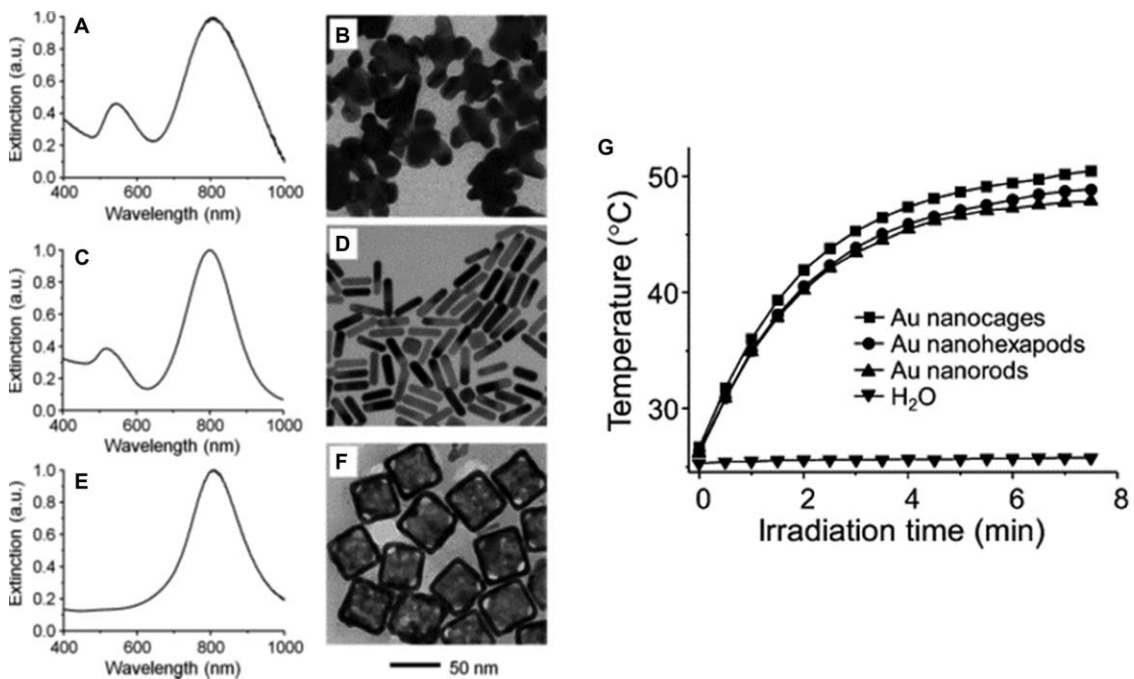
Figure 3.17 Absorption spectra and TEM images of Au nanohexapod (A and B), Au nanorods (C and D) and Au nanocages (E and F) for comparison of photothermal effect; (G) temperature elevation of water when the nanostructures are subjected to irradiation of an 805 nm laser at 0.8 W cm^{-2} power density.
Reproduced from ref. 127 with permission from American Chemical Society, Copyright 2013.
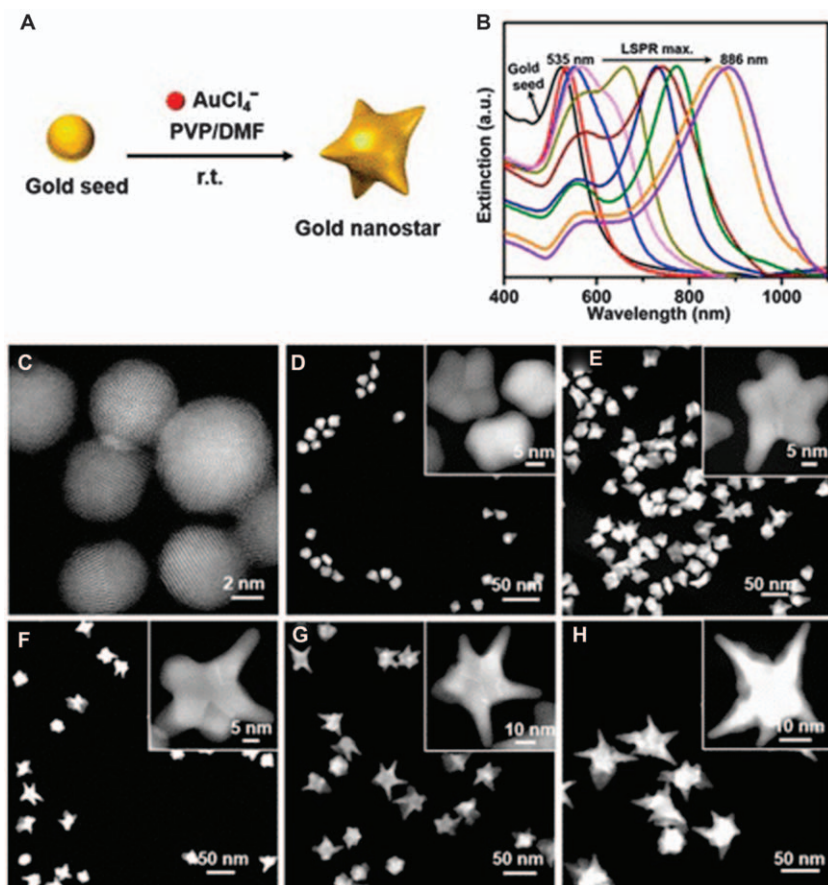
Figure 3.18 (A) Schematic illustration of the preparation of Au nanostars. Gold seeds serve as the nucleation site for the anisotropic growth of Au nanostars through the reduction of $AuCl_4^-$ in the presence of PVP and DMF. (B) Absorption spectra for the gold seed and Au nanostars with various concentrations of gold seeds and their corresponding HAADF-STEM images (C–H). Insets in (D–H) show STEM images of Au nanostars at a higher magnification.
Reproduced from ref. 133 with permission from American Chemical Society, Copyright 2018.

3.4 Applications of Branched Metallic Nanocrystals in Photothermal Therapy (PTT)

With the advancement of nanotechnology, the idea of using heat as a treatment option has been re-evaluated and modified to progress into next generation therapeutics. In this development, inorganic nanostructures have attracted special interest due to their high thermal conversion efficiency, application in bio-imaging, ease of synthesis and surface modification. Among these, plasmonic noble metallic nanostructures distinguish themselves from

other nanostructures such as semiconductor quantum dots, and magnetic and polymeric nanoparticles by their unique surface plasmon resonance (SPR). This SPR, resulting from photon confinement to a small particle size, enhances all the radiative and nonradiative properties of the nanoparticles.

The conventional cancer treatment regimens include surgical resection, radiation therapy, and chemotherapy, where the latter two tend to have side-effects and damage normal tissues. On the other hand, multidrug-resistant organisms (MDROs) are on the rise at an alarming rate around the world. Infections due to MDROs are extremely hard to treat as MDROs are resistant to many antibiotics in the frontline, making treatments ineffective. These problems call for attention and alternative treatment options. To reduce risks/side effects and avoid drug resistance, new medical strategies such as photothermal sensitization and photothermal ablation therapy have been explored for cancer management and infection treatment. Nanotechnology brings excitement for cancer diagnosis and therapy as well as MDRO infection treatment through heat generated from light to destroy cancer or MDRO cells, without affecting the surrounding healthy normal tissues. For the success of photothermal treatment, strong optical absorption of metallic nanostructures and their high efficiency of photothermal conversion, as well as their active accumulation at the sites are critical.

Plasmonic photothermal therapy involving gold-based nanoparticle contrast agents was first reported by Pitsillides and group in 2003.[134] They used anti-CD8 immunogold nanospheres in combination with a nanosecond visible pulsed laser. These nanoparticles specifically bound to T lymphocyte cells and subsequent laser irradiation resulted in destruction of over 90%. Later, Zharov *et al.*[135] reported that cancer cell death could be induced by a single nanosecond pulse at an energy of 2–3 J cm^{-2} with 10–15 gold nanoparticles per cell. However, visible light does not penetrate tissue optimally in clinical applications. Thus, NIR light is required for its deep penetration due to minimal absorption of the hemoglobin and water molecules in tissues in this spectral region. Along with it, NIR-absorbing metal nanoparticles are required. Extensive studies have addressed the issue through various perspectives including but not limited to tuning shape, size, and composition to develop metal nanostructures to achieve optimal structural and photothermal properties, as discussed in previous sections. Great efforts have been made to develop photothermal therapy strategies as alternative or combinational treatment options for diseases including cancer and infections caused by multi-drug-resistant bacteria and bacterial biofilm.[136]

Due to unique strong surface plasmon resonance (SPR) absorption, noble metals such as gold and silver nanostructures can significantly enhance photothermal conversion and are promising for photothermal therapy applications. Ideally, metal nanostructures should have strong and tunable SPR, be easy to deliver, have low toxicity, and be convenient for bioconjugation for actively targeting specific cells.[137] Here, we would highlight the importance of shape in achieving photothermal properties with the focus on gold branched nanostructures for photothermal applications in cancer and infection management.

3.4.1 Cancer Management

Most chemotherapeutic drugs are not specific to tumor cells, but are also able to cause harm to other cells and consequently are associated with side effects such as compromised immunity, hair loss, nausea, *etc.* In the pursuit of therapies capable of reducing undesired side effects and enhancing efficacy, there has been growing interest in utilizing hyperthermia (heat) to achieve these goals.[138] The history of using hyperthermic cancer therapy originated in 1893 by Coley; cancer patients infected by erysipelas had high fevers and resulted in either reduced cancer symptoms or complete regression of tumors.[139] Since then, studies have been performed applying hyperthermia to cancerous tumors to maintain tissue temperatures of 42 to 45 °C for treatment.[140] As whole body hyperthermia would cause cardiovascular and gastrointestinal side effects, a favorable modality for cancer treatment would require a targeted, nanoparticle-mediated localized hyperthermia.

One of the unconventional approaches is the use of NIR irradiation and heat-absorbing metal nanostructures to selectively and effectively eradicate cancer cells.[69,109] Such treatment using NIR light absorption to incite thermal damage is an established means of destroying cancer tissues since tissues heated beyond a certain thermal threshold undergo various mechanisms of cellular damage such as protein structural changes or carbonization of tissues.[141] Metal nanostructures perform as nanoscale heaters for photothermal therapy. Under specific light irradiation, photothermal therapy can be applied to localize heat focused on the target site to kill cancer cells at a specific part of the body in a non-invasive manner.

Gold nanostructures have found numerous medical applications in recent years because of their facile synthesis and surface modification, strongly enhanced and tunable optical properties, and most importantly their excellent biocompatibility making it feasible for clinical settings. Besides these attractive properties, synthesis methods of gold nanostructures have also been modified to be more favorable. High quality, high yield, and size controllable colloidal branched gold nanostructures can be quickly prepared by greener synthesis methods.[142]

The successful fabrication of structurally more complex metal nanostructures such as semi-shells, multi-shells, split rings, helixes, and gammadions has created greatly enriched surface plasmonic properties.[143] Metallic nanostructures with their geometry-dependent optical resonances are of great interest due to their ability to manipulate light in ways not possible with conventional optical materials.[144] The morphology and size of the nanostructures strongly affect their surface plasmon resonance (SPR) properties and subsequently influence their applications.[145] For instance, gold nanorods or nanostars are more suitable for photothermal therapy than spherical gold nanoparticles, owing to their shape. As they comprise branches, they can absorb incident NIR light more efficiently and thus achieve higher light-to-heat conversion, giving rise to better heat generation.
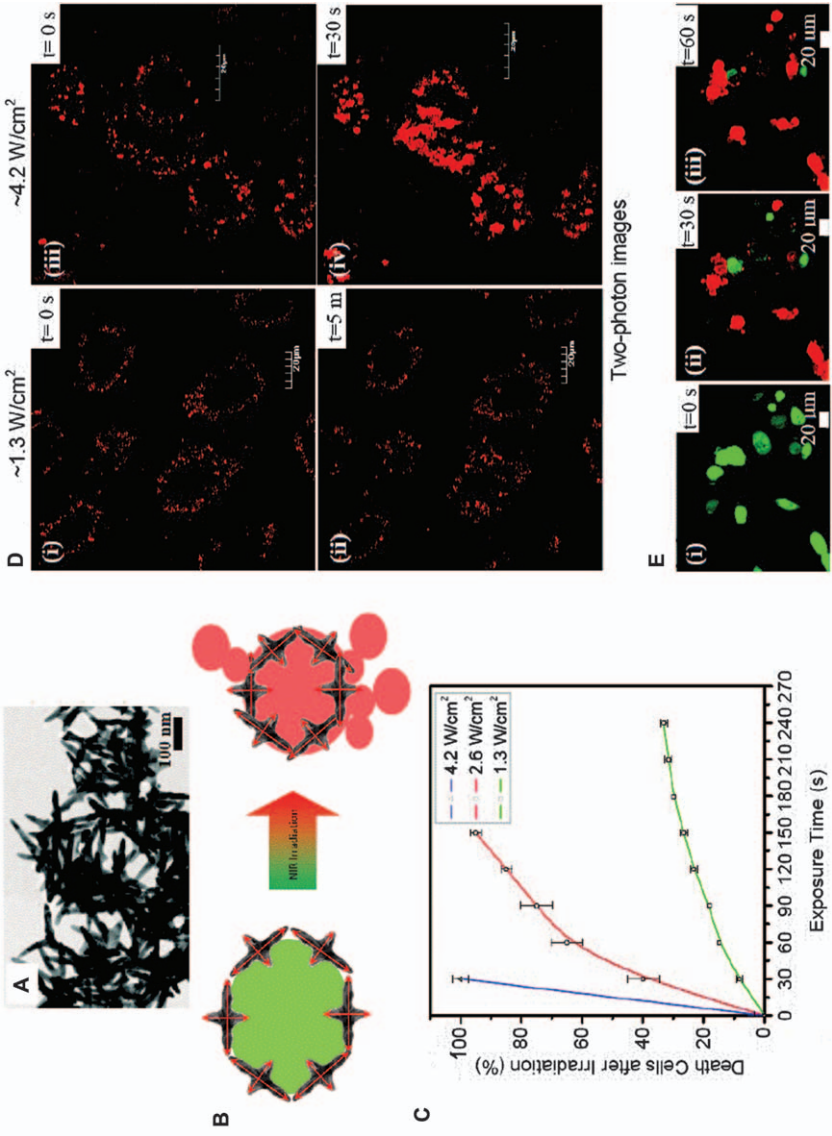
The branched gold nanostructures have inspired wide research interests
due to their good biocompatibility and excellent photothermal property.
Taking these factors into consideration in the design and development of
photothermal tools, Ye and colleagues[109] devised free-standing multiple-
branched gold nanocrosses which exhibit a pronounced near- and mid-IR
localized surface plasmon resonance (LSPR). Structural analysis showed
singly and doubly twinned gold nanocrosses (see Figure 3.16). These highly
multiple-branched gold nanocrosses, as seen in Figure 3.19A, produced a
rich surface plasmon spectrum, demonstrating that the effective conversion
of NIR light into heat mainly relied on their branched features. Notably, gold
nanocrosses act as an octopus antenna in efficiently capturing the incident
light along any branches and convert it into heat which is then rapidly
transmitted to the localized area and destroys cancer cells effectively.

A comprehensive study revealed the effect of laser intensity and exposure
time on the destruction of cells *via* irradiation of human lung cancer cells
(A549 cells) associated with gold nanocrosses using a 900 nm laser at in-
tensities of 1.3, 2.6, and 4.2 $W\,cm^{-2}$ (see Figure 3.19C). Remarkably, all the
cancer cells were killed under laser irradiation within 30 s at 4.2 $W\,cm^{-2}$
while ∼95% of the cells were killed after laser irradiation for 150 s at
2.6 $W\,cm^{-2}$. However, cell death was not observed in control experiments in
the absence of gold nanocrosses, where the cancer cells remained alive even
after 10 min of irradiation. For qualitative study of the photothermal treat-
ment, cells were also observed under a confocal microscope. At a lower laser
intensity of ∼1.3 $W\,cm^{-2}$, gold nanocrosses associated primarily on the A549
cells and were observed to have minimal changes in shape after 5 min of
irradiation. But at a higher laser intensity of 4.2 $W\,cm^{-2}$, the cells started
to shrink immediately upon laser exposure. These observations are well
correlated to the quantitative study (see Figure 3.19D). After 30 s irradiation
at 4.2 $W\,cm^{-2}$, the cells had drastically been changed in both shape and size.
The resulting collapsed cell membranes affected the gold nanocrosses and
agglomerates were observed. Furthermore, the time-dependent damage
process under irradiation at a middle laser intensity of 2.6 $W\,cm^{-2}$ (see
Figure 3.19E) illustrated a slower destruction rate, as predicted.

Figure 3.19 Photothermal damage, Arrhenius model, and two-photon lumines-
cence imaging of A549 cancer cells associated with gold nanocrosses.
(A) TEM image of gold nanocrosses. (B) A schematic of the destruction
of cancer cells by gold nanocrosses under NIR laser irradiation. Gold
nanocrosses accumulate on the surface of cancer cells, then convert the
incident light into heat and destroy cancer cells upon NIR irradiation.
(C) Photothermal damage of A549 cancer cells associated with gold
nanocrosses as a function of time at 900 nm laser intensities of 1.3, 2.6,
and 4.2 $W\,cm^{-2}$. (D) Confocal images showing the time-dependent
damage process at 2.6 $W\,cm^{-2}$ after 900 nm irradiation for 0, 30, and
60 s. (E) Two-photon luminescence images of gold nanocrosses associ-
ated with cells under 900 nm laser excitation at 1.3 and 4.2 $W\,cm^{-2}$.
Reproduced from ref. 109 with permission from American Chemical
Society, Copyright 2011.

The study indicates that the shape of nanostructures significantly influences their absorption efficiency and photothermal profile. Similarly, laser intensity and irradiation time greatly affect the success of photothermal treatment. The synergistic coupling between the branches facilitates the highly branched gold nanocrosses to efficiently capture IR light for effective photothermal destruction of cancer cells. The enhanced hyperthermia properties of the gold nanocrosses proved to be a very promising tool for cancer therapy. An effective targeted-therapy method, combined with laser-induced hyperthermia therapy, could be an alternative way to treat solid tumors.[146–148]

As the temperature elevation is directly related to the absorption of light by plasmonic nanostructures, the absorption cross-section of nanostructures of different shapes is important criteria in the design of plasmonic nanostructures. Gold nanostructures with controlled assembly could bring in tunable optical and photothermal properties. Gold nanoflowers (GNF) using 'green' L-ascorbic acid has caught attention as they have abundant petals giving a large absorption cross-section and these nanoflower petals play an important role in Raman signal enhancement allowing signal improvement in the order of 10^6. This enhancement was explained in terms of the electromagnetic enhancement mechanism of the metal nanomaterials.[149] These gold nanoflowers demonstrated high biocompatibility and improved signals when using a confocal microscope, indicating its applicability as a multimodal *in vitro* SERS-based sensor and imaging tag. In another study, GNF produced using starfruit juice showed interesting NIR photothermal properties.[69] This suggests that the GNFs produced can be used as a photothermal therapy agent as the biomolecules in the starfruit juice cap the GNFs and make them more biocompatible. Next, irradiation time effect on the photothermal destruction of the MCF-7 cancer cells was investigated by confocal microscopy throughout the laser irradiation. Obviously, the cells started to bleb after a few seconds of irradiation and were destroyed after 30 s (see Figure 3.20A). Dead cells with a blebbing membrane indicate that the destruction of the cancer cells might be due to localized heat at their membrane which was in direct contact with GNFs. The highly efficient *in vitro* photothermal therapy led to further investigation of the *in vivo* photothermal therapy using MCF-7 tumor-induced BALB/c mice and 808 nm NIR laser irradiation at a power density of 0.5 W cm^{-2} for 6 min. Tumors shrank and eventually disappeared in the mice with GNF injection and laser irradiation while tumors grew rapidly in the mice with either NIR irradiation without GNF injection, or GNF injection without NIR irradiation (see Figure 3.20B–D). The results indicate that either NIR irradiation or GNF injection alone did not provide any therapeutic effect on the tumor, demonstrating an excellent *in vivo* photothermal therapeutic efficacy of GNFs. Gold nanoflowers present great potential in photothermal cancer therapy.

The shape-dependency of photothermal properties is well pronounced. The highly branched gold nanostructures with sharp tips – nano-snowflakes hold the highest photothermal conversion efficiency, and gold nanostructures with blunt tips – nanoflowers hold the lowest.[151] Gold nano-snowflakes could absorb light with a wide range of wavelengths from 500 nm to more
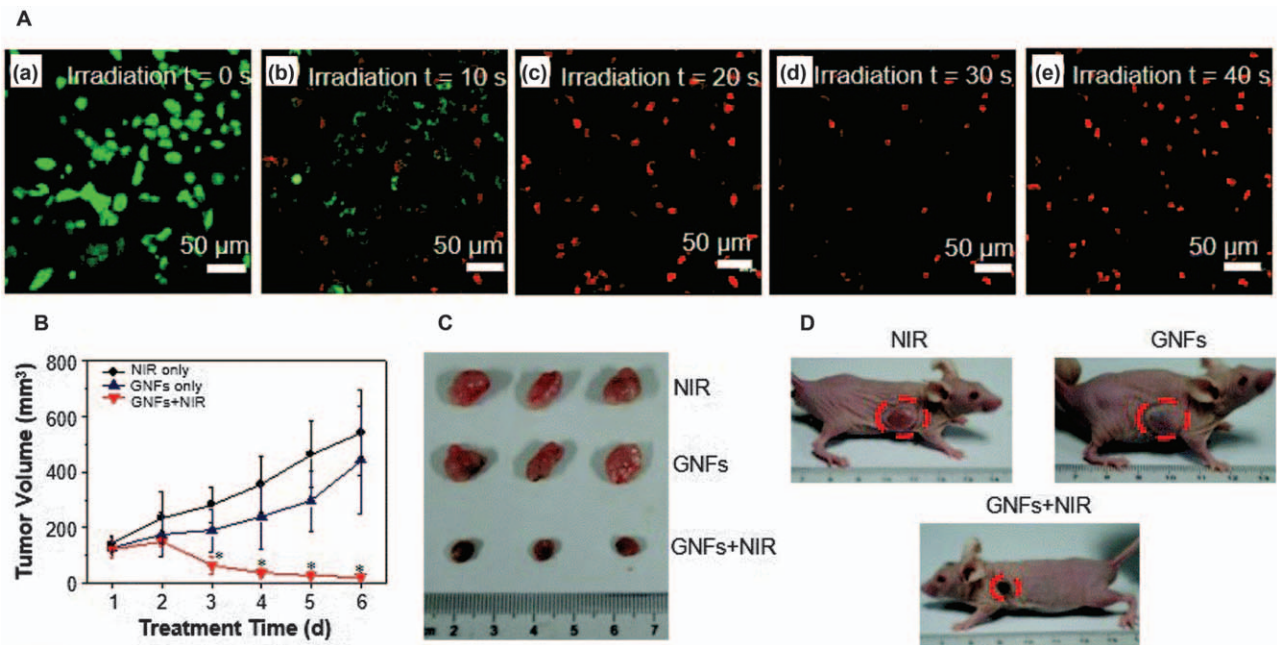
Figure 3.20 Photothermal destruction of MCF-7 cancer cells using GNFs. (A) Confocal microscope images demonstrating the effect of irradiation time on the photothermal destruction of MCF-7 cells incubated with GNFs under irradiation with an 808 nm CW laser. (B) *In vivo* evaluation of the photothermal therapy of tumor by GNFs under NIR irradiation. Initial dorsal subcutaneous tumor implantation was conducted by injecting MCF-7 cancer cells into mice. The experiments started when the tumor size reached ~110 mm^3. The experimental results are shown as a mean with the SD error bars ($n = 5$). (C) The images of excised tumors from different groups after treatment for 6 days. (D) Representative photographs of mice with treatment of the NIR laser only, GNFs only, and GNFs under NIR laser irradiation after 6 days.
Reproduced from ref. 69 with permission from the Royal Society of Chemistry.

than 1000 nm which covered the visible light to near infrared region due to their highly branched structure. The highest photothermal conversion efficiency of gold nano-snowflakes may be attributed to: the wider SPR absorption peak with high absorption around 808 nm and highly branched nanostructure for enhancing the local electromagnetic field of petals on the surface. The red-shift and much wider SPR absorption peak is consistent with the shape evolution from gold nanoflowers to nanostars and finally to nano-snowflakes. Gold nanostars have two localized SPR (LSPR) peaks in the visible and infrared regions; their Raman signal enhancement and SERS ability greatly depend on the infrared absorption from the plasmon resonance along the aligned branches. The lightning rod effect and creation of hot spots could be enhanced with the length and number of gold branches.[152]

Besides the shape, the size of nanostructures strongly influences their photothermal effects on cells.[134,135] Nanostructures with sizes from 10 to 30 nm have the strongest effect.[153] Although theoretical calculations may indicate that the photothermal effect of larger nanostructures is more significant, the lower cellular uptake might have reduced overall efficiency. Also, the size of 10–30 nm is very well correlated to microbubble formation, a cause of cell damage, induced by the nanostructures.

With high interest in developing innovative smart nanomedicines, there could be a whole range of different shapes and sizes of plasmonic branched nanostructures exhibiting strong photothermal efficacy, to emerge for evaluation in clinical settings. There are also hybrid photothermal nanostructures, incorporating different materials for improved stability, synergistic effects, enhanced efficacy, *etc.* For instance, by incorporating silver into gold, Ag–Au nanostructures exhibit a high SERS activity while incorporating an aptamer into Ag–Au nanostructures enables targeting the surface of human breast cancer cells (MCF-7 cells) with high affinity and specificity.[154] Collectively, the aptamer–Ag–Au nanostructures have a high adsorption of NIR irradiation and capability to execute photothermal therapy of MCF-7 cells at a very low irradiation power density (0.25 $W\,cm^{-2}$) without destroying the healthy cells and the surrounding normal tissue. These nanostructures may offer a protocol to specifically recognize and sensitively detect the cancer cells, and great potential for application in the photothermal therapy of the cancers.

As bimetallic nanostructures draw attention as exciting materials for effective photothermal therapy, Joseph *et al.*[155] reported gold–silver (AuAg) spiky branched nanostars with gold (90%) being the major component, possessing two distinct intense localized surface plasmon resonances in the NIR and short-wavelength infrared ranges. AuAg nanostars with evenly spaced spikes and low branching expressed great potential for photothermal therapy, active in both the visible and NIR regions. McGrath and co-workers[156] developed palladium–gold (Pd–Au) nanostructures containing multiple gold nanocrystals on highly branched palladium seeds. Pd–Au heterostructures caused destruction of HeLa cancer cells *in vitro*, as well as complete destruction of tumor xenographs in mouse models *in vivo* under

808 nm laser irradiation at an intensity of 3 $W\,cm^{-2}$ for 30 min, demonstrating effective photothermal therapy (see Figure 3.21A–C). In contrast, there was no significant effect on cell viability or tumor site in the absence of the nanostructures or exposure to laser light.

To achieve biocompatibility, Xia's group[127] coated gold nanohexapods with polyethylene glycol and demonstrated application in photothermal therapy and diagnosis. The PEGylated Au nanohexapods achieved high cellular uptake and low cytotoxicity *in vitro* as well as significant blood circulation and tumor accumulation after intravenous injection *in vivo*. The PEGylated Au nanohexapods exhibited the highest photothermal conversion efficiency *in vivo* when
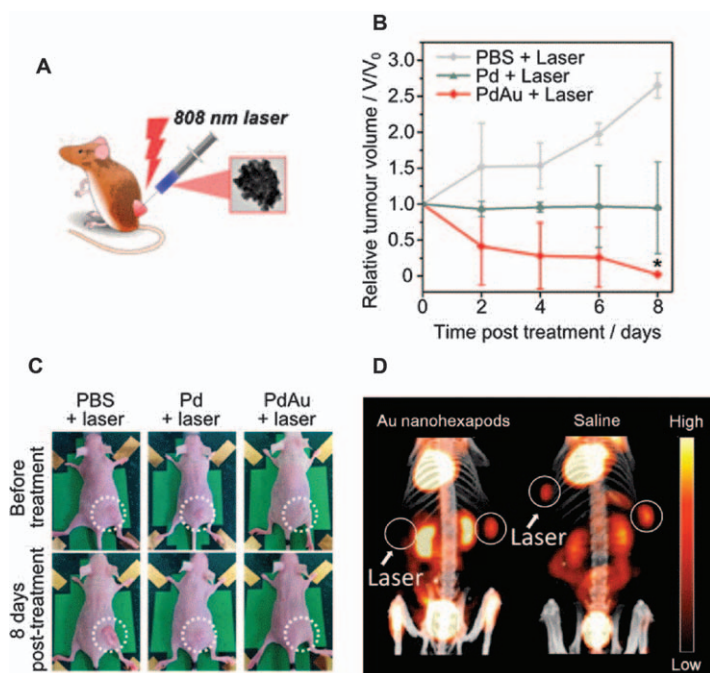

Figure 3.21 *In vivo* photothermal treatment using branched nanostructures. (A) Schematic of *in vivo* photothermal treatment. (B) *In vivo* photothermal hyperthermia efficacy of Pd–Au, as compared to laser treatment with Pd seeds and with PBS only. A quantity of 100 µL of either PBS, Pd, or Pd–Au (at 50 $\mu g\,mL^{-1}$ Pd concentration) in PBS was injected into HeLa xenographs in mice ($n = 3$ for each group; $*p < 0.05$). (C) Representative images taken of the mice immediately before and 8 days after laser irradiation of the tumor site for 30 min at 3 $W\,cm^{-2}$. The dashed white circles indicate the tumor regions. Reproduced from ref. 156 with permission from American Chemical Society, Copyright 2015. (D) ^{18}F-FDG PET/CT co-registered images of mice intravenously administered with an aqueous suspension of Au nanohexapods and saline solution. Tumor locations are marked with white circles. Irradiated tumors are highlighted with white arrows. Reproduced from ref. 127 with permission from American Chemical Society, Copyright 2013.

compared with PEGylated Au nanocages and Au nanorods, possibly due to
branched features. When the photothermal treatment effect on tumor meta-
bolic activity was assessed using ^{18}F-flourodeoxyglucose positron emission
tomography combined with computed tomography (^{18}F-FDG PET/CT),
significantly reduced ^{18}F-FDG uptake was found in the irradiated tumors in
contrast to the contralateral non-irradiated tumors (see Figure 3.21D). Photo-
thermal treatment presented 90% reduction of tumor metabolism in mice
treated with Au nanohexapods. This indicates branched Au nanostructures as
promising photothermal materials achieving almost complete destruction of
tumor glycolic activity.

For high stability in an isotonic solution, Lin et al.[157] linked branched-gold
nanoparticles with thiol-modified mannoside (Man@BAu NPs). Man@BAu
NPs showed low cytotoxicity, broad NIR absorption in the biological window,
and good photothermal conversion killing ~36–55% of the MDA-MB-231 cells
under 808 nm laser irradiation (1.08 W) for 10 min.

3.4.2 Bacterial and Biofilm Treatment

The widespread use of antibiotics has resulted in the ongoing and ever-
increasing occurrences of antibiotic-resistant bacteria. Antibiotic resistance
is a continually evolving process and has become a serious problem of global
public health. Relying on existing drugs to treat the bacterial diseases will
not be able to circumvent the development of resistance by bacteria.[158] Also,
bacteria may be developed into biofilm which can physically block the access
of drugs to the bacterial cells, making treatment even more difficult.[159]
Therefore, treatment of the emerging antibiotic-resistant bacteria requires a
totally new strategy that is conceptually different from the traditional small-
molecule drugs.[160] There is a strong interest in the use of plasmonic metal
nanoparticles for bacterial infection treatments through photothermal
therapy. As NIR light is reported to penetrate the subcutaneous cell layer up
to a depth of 10 mm to a few centimeters, the structural dimensions of metal
nanostructures are specifically designed to ensure that they maximally
absorb NIR light for subsequent effective conversion into heat.[161] These
significant properties have drawn attention to develop gold nanostructures
as novel and competent nano-photothermal vectors to destroy bacteria at the
molecular level, circumventing drug-resistant issues.

Plasmonic gold nanostructures are promising nanomedicines for combat-
ing drug resistant bacterial infections as they can absorb light efficiently in the
NIR region where light penetration in tissues is optimal and convert it to local
heat by photo-exciting the conduction electrons to induce surface plasmon
oscillations followed by non-radiative relaxation.[162] A significant photothermal
effect can be obtained using gold nanostructures at fluences below the medical
laser safety threshold[163] which is of the order of 20 to 100 mJ cm^{-2} depending
on the method of application. While NIR wavelengths harmlessly pass through
the human body, they heat plasmonic materials such as gold nanoshells to a
high temperature of more than 70 °C and will thermally ablate any cell

(bacteria or eukaryotic) in close proximity to these plasmonic materials. The advantage of this treatment method is selective killing of the cells in direct contact with gold nanostructures but leaving surrounding healthy cells unaffected, owing to the rapid dissipation of thermal energy over short distances.

Heat radiation is very promising to effectively address the issue of antibiotic resistance because it can be easily delivered to the infected sites for physically destroying bacteria instead of inhibiting their growth like drugs. The temperature at the targeted region has to reach between 40 and 50 °C in order to kill cancer cells while for bacteria and biofilm the temperature has to reach between 50 and 80 °C as bacteria have double cell walls which need higher energy for their destruction.[164] Various types of gold nanostructures were explored for ablation of multidrug-resistant bacteria and biofilms at the infected area.[125,165–168]

Thermal ablation of bacteria using plasmonic gold nanostructures depends largely on the efficiency of NIR light absorption, distribution of nanostructures at the target site, and temperature profile upon laser irradiation.[169] To enhance stability and targeting ability, gold nanostructures can easily be modified with appropriate surface ligands *via* the surface chemistry of gold. Teng and colleagues[125] conjugated NIR-absorbing gold nanocrosses with biologically active moieties to achieve targeting to the pathogenic bacteria *P. aeruginosa* PAO1 selectively for complete destruction of the bacteria and their biofilm. When exposed to 800 nm light with a low power density of 3.0 W cm^{-2} for 5 min, the conjugated gold nanocrosses were heated up promptly and destructed the superbug bacteria completely (see Figure 3.22). The local hyperthermia is achieved *via* functionalized plasmonic gold nanocrosses which efficiently convert optical energy into thermal energy upon irradiation with light for photo-ablation of bacteria in a short time, and all the cells deceased under 70 °C for 5 min or 80 °C for 2 min. Complete ablation was observed in the irradiated region of the biofilm marked with a dashed line, while the surrounding cells beyond the laser-exposed area remained alive. It shows that all the biofilm cells in the area irradiated with the laser were killed while the biofilm cells beyond the laser-exposed area have no noticeable effect, indicating the localized photothermal effect. Even after 48 h post-irradiation, there was no live bacteria present. This indicates that the hyperthermia is a promising tool for ablating bacteria and inhibiting the development of biofilm.

The localized hyperthermia is shown to be highly shape- and composition-dependent and can be tuned to achieve efficient photothermal activities in the desired applications. The gold nanostars in colloidal solutions demonstrated efficient photothermal properties of 3 and 100 times higher than gold nanorods and iron oxide nanoparticles, respectively.[170] Borzenkov and co-workers[171] embedded gold nanostars in thin PVA films to display improved mechanical properties and an enhanced photothermal activity. The films showed promising photothermal activities upon exposure to NIR light, offering novel bactericidal films with a protective function. Similarly, monolayers of gold nanostars were attached onto mercaptopropyltrimethoxysilane-modified
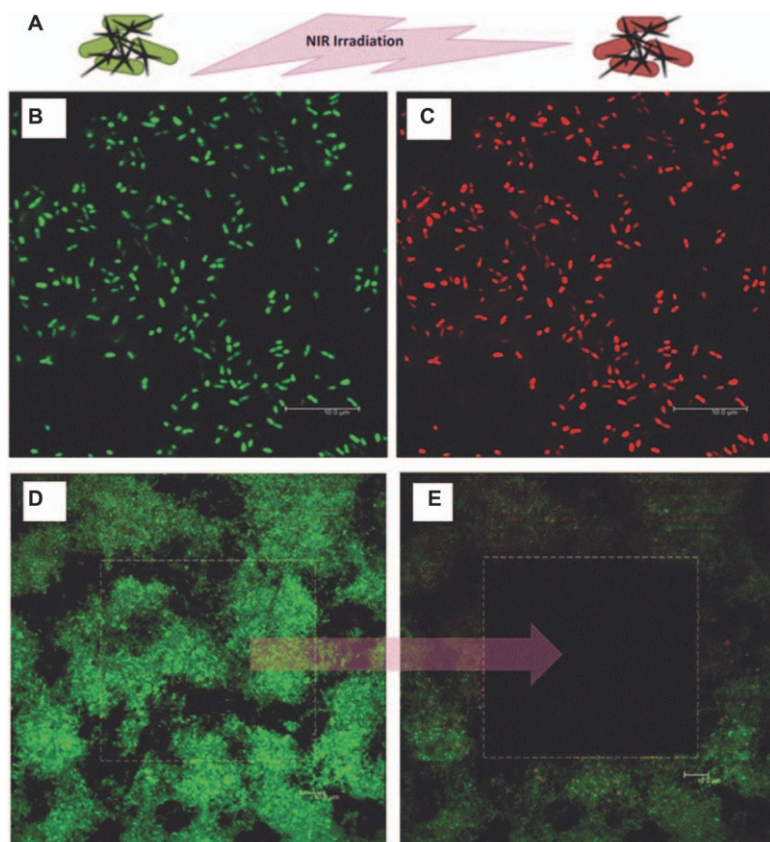
Figure 3.22   Photothermal effect of the conjugated gold nanocrosses on the growth of PAO1 bacteria and biofilm. (A) Schematic of photothermal treatment of bacterial infection using conjugated gold nanocrosses and NIR laser irradiation. Confocal images of PAO1 bacteria preincubated with the conjugated gold nanocrosses (B) before irradiation and (C) after irradiation for 5 min with a multiphoton laser at 800 nm at a power density of $\approx$3.0 W cm^{-2}. Bacteria destruction was indicated by red staining with propidium iodide and no destruction (no adverse effect) was indicated by green staining with syto 9. Confocal images of the biofilm treated with gold nanocrosses (D) before irradiation and (E) after irradiation at its central rectangular region for 5 min with a multiphoton laser at 800 nm at a power density of $\approx$3.0 W cm^{-2}. Localized photothermal effect and ablation of the biofilm were observed in the irradiated region. Confocal imaging was performed at 100$\times$ magnification. Scale bar = 10 μm.
Reproduced from ref. 125 with permission from John Wiley and Sons, Copyright © 2016 WILEY-VCH Verlag GmbH & Co. KGaA, Weinheim.

glass substrates to provide a photothermal platform for generating local hyperthermia and effectively destroying *S. aureus* biofilms.[172]

Gold nanoflowers with a strong NIR plasmon may serve as an efficient photothermal agent in antibacterial applications. Gold nanoflowers with

their surface protrusions offer a larger surface area for surface functionalization. These would direct them to bacteria, resulting in cell death and other cellular damage *via* the rupture of the cellular membrane of bacteria. When comparing the bactericidal effects of gold nanoparticles, nanostars, and nanoflowers toward *S. aureus* bacteria, it is evident that antibacterial activity is dependent on the shape of the gold nanostructures. Gold nanoflowers exhibited the most promising performance in various anti-infection applications accompanied with non-cytotoxic function to mammalian cells.[173] Stable Dap-Au nanoflowers were prepared with daptomycin (Dap) micelles as the template and reducing agents to generate a photothermal conversion efficiency of ~40% from light to heat and effectively inhibit the growth of bacteria in the assistance of 808 nm light.[174]

Although silver is known as a highly-effective and broad-spectrum antibacterial agent, its severe cytotoxicity to mammalian cells and noticeable reduction in antibacterial activity with time restrict their practical applications. For better application prospects, bimetallic gold–silver particles were recently developed for improved application in photothermal and antibiotic-based treatment as compared to pure gold or silver particles. This enhanced bactericidal activity without increasing their cytotoxicity guarantees the clinical applications of silver.[175] Encouraged by this, the development of many other hybridized photothermal nanostructures is in the pipeline to serve in photothermal therapy applications.

3.5 Conclusion, Perspective, and Outlook

In recent years, there has been mounting interest in using branched metallic nanocrystals for photothermal applications. As the shape, size, and morphology of the nanocrystals have a vast impact on their properties and applications, interest in the synthetic routes that ensure careful control of such nanostructures is also growing rapidly. In this chapter, four traditional solution-based strategies (seeded growth, seedless growth, templated growth, and chemical etching), with a recent growing green method are discussed. Seeded growth, the oldest method of the lot, involves a two-step process that first grows small metal nanocrystals. They are then used as seeds for further formation of branches on the nanocrystals due to the different surfaces. This strategy allows precise control in size due to the splitting of nucleation and growth stages. Moreover, the final morphology of the anisotropic nanostructures can also be controlled by the shape, size, and composition of the seed. This approach also allows the formation of bimetallic nanostructures easily. Seedless growth, on the other hand, does not use pre-synthesized seeds to facilitate the subsequent branching, instead, foreign ions or capping agents are added to mediate its growth. Crystal twinning and polymorphism are also exploited for such growth, hence, seedless growth is a convenient one-pot synthetic strategy. The templated growth strategy, as the name implies, uses a template to facilitate the nucleation and direct the growth of branched nanostructures. Materials like deep eutectic solvents and

nanoparticle arrays are some examples that are used as such templates. The chemical etching route uses chemical etchants to selectively dissolve certain crystallographic facets to achieve branched nanoarchitectures. Lastly, there has been a tremendous development in using green methods for anisotropic growth of branched nanostructures. Biogenic substances like plant extracts, microorganisms, and biomolecules are used in the synthesis for reasons such as being more environmentally friendly and biocompatible. This allows the synthesized branched metallic nanocrystals to be a safer option for biomedical applications.

With the synthesized anisotropically branched nanostructures, the properties of the nanocrystals were studied for better fit for various applications. For example, branched Au nanostructures provide pronounced absorption in the NIR region, which could be further exploited for photothermal ablation or photothermal-modulated drug release applications. While novel metallic nanostructures with superseding capabilities are increasingly developed, it is important to appreciate how the introduction of branched features could induce stronger NIR absorption and the corresponding photothermal effect.

As discussed, the applications of photothermal therapy for cancer and bacterial and biofilm treatments are almost limited to the use of Au and Ag nanostructures. They both have superior plasmonic and photothermal properties but can be costly as they are noble metals. However, Au is mostly preferred due to its stability even though Ag is relatively cheaper and has a stronger plasmonic response. It is postulated that Ag will make a good alternative to Au by functionalizing the branched Ag nanostructures, making them more stable. Alloyed anisotropic nanocrystals containing Au and Ag could also be further studied to capture the advantages of both metals.

Prospectively, we envision that more versatile and facile methods will be developed for the synthesis of anisotropic metal nanostructures. This allows more cutting-edge nanostructures to be designed for explicit applications with particular properties. However, growth mechanisms and structure-to-property correlations need to be studied in depth to be accelerated for wider applications of such materials. Additionally, the formation of nanostructures using different types of metals can also be explored. Currently, the most commonly used metals include Au, Ag, Pt, and Pd. With more different types of branched metallic nanocrystals, new properties and applications may be viable. Furthermore, we foresee a huge growth in synthesis of anisotropic metallic nanocrystals *via* biogenic methods. Biogenic synthesis ensures that the nanostructures are benign and safe for biomedical application. Last but not least, challenges related to stability and scaling-up need to be overcome to enable branched metallic nanocrystals to be commercialized for such applications.

Uncited Reference

150

References

1. E. C. Dreaden, A. M. Alkilany, X. Huang, C. J. Murphy and M. A. El-Sayed, *Chem. Soc. Rev.*, 2012, **41**, 2740–2779.
2. M. Hu, J. Chen, Z. Y. Li, L. Au, G. V. Hartland, X. Li, M. Marquez and Y. Xia, *Chem. Soc. Rev.*, 2006, **35**, 1084–1094.
3. P. K. Jain, X. Huang, I. H. El-Sayed and M. A. El-Sayed, *Acc. Chem. Res.*, 2008, **41**, 1578–1586.
4. K. Xia, L. Zhang, Y. Huang and Z. Lu, *J. Nanosci. Nanotechnol.*, 2015, **15**, 63–73.
5. S. Cheong, J. D. Watt and R. D. Tilley, *Nanoscale*, 2010, **2**, 2045–2053.
6. H. Zhang, M. Jin, Y. Xiong, B. Lim and Y. Xia, *Acc. Chem. Res.*, 2013, **46**, 1783–1794.
7. S. Pal, Y. K. Tak and J. M. Song, *Appl. Environ. Microbiol.*, 2007, **73**, 1712–1720.
8. M. Faraday, *Philos. Trans. R. Soc.*, 1857, **147**, 145–181.
9. A. R. Tao, S. Habas and P. Yang, *Small*, 2008, **4**, 310–325.
10. Y. Xia, Y. Xiong, B. Lim and S. E. Skrabalak, *Angew. Chem., Int. Ed.*, 2009, **48**, 60–103.
11. B. Lim and Y. Xia, *Angew. Chem., Int. Ed.*, 2011, **50**, 76–85.
12. H. You, S. Yang, B. Ding and H. Yang, *Chem. Soc. Rev.*, 2013, **42**, 2880–2904.
13. W. Niu, L. Zhang and G. Xu, *Nanoscale*, 2013, **5**, 3172–3181.
14. C. Gao, J. Goebl and Y. Yin, *J. Mater. Chem. C*, 2013, **1**, 3898–3909.
15. N. R. Jana, L. Gearheart and C. J. Murphy, *Adv. Mater.*, 2001, **13**, 1389–1393.
16. T. K. Sau and C. J. Murphy, *Langmuir*, 2004, **20**, 6414–6420.
17. D. Y. Kim, T. Yu, E. C. Cho, Y. Ma, O. O. Park and Y. Xia, *Angew. Chem., Int. Ed.*, 2011, **50**, 6328–6331.
18. C. J. Desantis, A. A. Peverly, D. G. Peters and S. E. Skrabalak, *Nano Lett.*, 2011, **11**, 2164–2168.
19. C. J. DeSantis, A. C. Sue, M. M. Bower and S. E. Skrabalak, *ACS Nano*, 2012, **6**, 2617–2628.
20. R. G. Weiner, C. J. DeSantis, M. B. T. Cardoso and S. E. Skrabalak, *ACS Nano*, 2014, **8**, 8625–8635.
21. P. Senthil Kumar, I. Pastoriza-Santos, B. Rodriguez-Gonzalez, F. Javier Garcia de Abajo and L. M. Liz-Marzan, *Nanotechnology*, 2008, **19**, 015606.
22. C. G. Khoury and T. Vo-Dinh, *J. Phys. Chem. C*, 2008, **112**, 18849–18859.
23. S. Maksimuk, X. Teng and H. Yang, *J. Phys. Chem. C*, 2007, **111**, 14312–14319.
24. H. Zhang, X. Xia, W. Li, J. Zeng, Y. Dai, D. Yang and Y. Xia, *Angew. Chem., Int. Ed.*, 2010, **49**, 5296–5300.
25. J. L. Elechiguerra, J. Reyes-Gasga and M. J. Yacaman, *J. Mater. Chem.*, 2006, **16**,
26. E. Ye, M. D. Regulacio, M. S. Bharathi, H. Pan, M. Lin, M. Bosman, K. Y. Win, H. Ramanarayan, S. Y. Zhang, X. J. Loh, Y. W. Zhang and M. Y. Han, *Nanoscale*, 2016, **8**, 543–552.

AQ:6

27. L.-C. Cheng, J.-H. Huang, H. M. Chen, T.-C. Lai, K.-Y. Yang, R.-S. Liu, M. Hsiao, C.-H. Chen, L.-J. Her and D. P. Tsai, *J. Mater. Chem.*, 2012, **22**, 2244–2253.

28. T. Herricks, J. Chen and Y. Xia, *Nano Lett.*, 2004, **4**, 2367.

29. X. Huang, Z. Zhao, J. Fan, Y. Tan and N. Zheng, *J. Am. Chem. Soc.*, 2011, **133**, 4718–4721.

30. G. T. Fu, X. Jiang, R. Wu, S. H. Wei, D. M. Sun, Y. W. Tang, T. H. Lu and Y. Chen, *ACS Appl. Mater. Interfaces*, 2014, **6**, 22790–22795.

31. J. Watt, N. Young, S. Haigh, A. Kirkland and R. D. Tilley, *Adv. Mater.*, 2009, **21**, 2288–2293.

32. J. Xie, J. Y. Lee and D. I. C. Wang, *Chem. Mater.*, 2007, **19**, 2823.

33. H. Liu, Y. Xu, Y. Qin, W. Sanderson, D. Crowley, C. H. Turner and Y. Bao, *J. Phys. Chem. C*, 2013, **117**, 17143–17150.

34. C. Wang, G. Xiao, Y. Sui, X. Yang, G. Liu, M. Jia, W. Han, B. Liu and B. Zou, *Nanoscale*, 2014, **6**, 15059–15065.

35. N. Ortiz and S. E. Skrabalak, *Angew. Chem., Int. Ed.*, 2012, **51**, 11757–11761.

36. A. P. LaGrow, S. Cheong, J. Watt, B. Ingham, M. F. Toney, D. A. Jefferson and R. D. Tilley, *Adv. Mater.*, 2013, **25**, 1552–1556.

37. Z. Li, W. Li, P. H. Camargo and Y. Xia, *Angew. Chem., Int. Ed.*, 2008, **47**, 9653–9656.

38. M. Zhu, B. Lei, F. Ren, P. Chen, Y. Shen, B. Guan, Y. Du, T. Li and M. Liu, *Sci. Rep.*, 2014, **4**, 5259.

39. V. S. Marangoni, L. D. Germano, C. C. C. Silva, E. A. de Souza and C. M. Maroneze, *Nanoscale*, 2018, **10**, 13315–13319.

40. H. G. Liao, Y. X. Jiang, Z. Y. Zhou, S. P. Chen and S. G. Sun, *Angew. Chem., Int. Ed.*, 2008, **47**, 9100–9103.

41. M. J. Mulvihill, X. Y. Ling, J. Henzie and P. Yang, *J. Am. Chem. Soc.*, 2010, **132**, 268.

42. L. Ma, C. Wang, M. Gong, L. Liao, R. Long, J. Wang, D. Wu, W. Zhong, M. J. Kim, Y. Chen, Y. Xie and Y. Xiong, *ACS Nano*, 2012, **6**, 9797.

43. S. Cheong, J. Watt, B. Ingham, M. F. Toney and R. D. Tilley, *J. Am. Chem. Soc.*, 2010, **131**, 14590.

44. M. S. Akhtar, J. Panwar and Y.-S. Yun, *ACS Sustainable Chem. Eng.*, 2013, **1**, 591–602.

45. M. A. Faramarzi and A. Sadighi, *Adv. Colloid Interface Sci.*, 2013, **189–190**, 1–20.

46. H. P. Borase, B. K. Salunke, R. B. Salunkhe, C. D. Patil, J. E. Hallsworth, B. S. Kim and S. V. Patil, *Biotechnol. Appl. Biochem.*, 2014, **173**, 1–29.

47. A. D. Brumbaugh, K. A. Cohen and S. K. St Angelo, *ACS Sustainable Chem. Eng.*, 2014, **2**, 1933–1939.

48. R. I. Iyer and T. Panda, *J. Nanosci. Nanotechnol.*, 2014, **14**, 2024–2037.

49. S. Poulose, T. Panda, P. P. Nair and T. Theodore, *J. Nanosci. Nanotechnol.*, 2014, **14**, 2038–2049.

50. J. Huang, L. Lin, D. Sun, H. Chen, D. Yang and Q. Li, *Chem. Soc. Rev.*, 2015, **44**, 6330–6374.

51. P. Dauthal and M. Mukhopadhyay, *Ind. Eng. Chem. Res.*, 2016, **55**, 9557–9577.
52. F. Qazi, Z. Hussain and M. N. Tahir, *RSC Adv.*, 2016, **6**, 60277–60286.
53. R. S. Varma, *ACS Sustainable Chem. Eng.*, 2016, **4**, 5866–5878.
54. P. Vishnukumar, S. Vivekanandhan and S. Muthuramkumar, *Chem-BioEng Rev.*, 2017, **4**, 18–36.
55. J. Singh, T. Dutta, K. H. Kim, M. Rawat, P. Samddar and P. Kumar, *J. Nanobiotechnol.*, 2018, **16**, 84.
56. G. A. Kahrilas, L. M. Wally, S. J. Fredrick, M. Hiskey, A. L. Prieto and J. E. Owens, *ACS Sustainable Chem. Eng.*, 2014, **2**, 367–376.
57. Y. Liu, S. Kim, Y. J. Kim, H. Perumalsamy, S. Lee, E. Hwang and T. H. Yi, *Int. J. Nanomed.*, 2019, **14**, 2945–2959.
58. N. Thangamani and N. Bhuvaneshwari, *Chem. Phys. Lett.*, 2019, **732**.
59. P. Vijaya Kumar, S. Mary Jelastin Kala and K. S. Prakash, *Mater. Lett.*, 2019, **236**, 19–22.
60. Y. Zheng, H. Zhang and L. Fu, *Inorg. Nano-Met. Chem.*, 2019, **48**, 449–453.
61. M. Zhou, J. Yin, X. Zhao, Y. Fu, X. Jin, X. Liu and T. Jiao, *Colloids Surf., A*, 2020, **603**.
62. L. Wang, M. Imura and Y. Yamauchi, *CrystEngComm*, 2012, **14**.
63. L. Wu, W. Wu, X. Jing, J. Huang, D. Sun, T. Odoom-Wubah, H. Liu, H. Wang and Q. Li, *Ind. Eng. Chem. Res.*, 2013, **52**, 5085–5094.
64. D. Sun, G. Zhang, J. Huang, H. Wang and Q. Li, *Materials*, 2014, **7**, 1360–1369.
65. D. Sun, G. Zhang, X. Jiang, J. Huang, X. Jing, Y. Zheng, J. He and Q. Li, *J. Mater. Chem. A*, 2014, **2**, 1767–1773.
66. X. Jing, D. Huang, H. Chen, T. Odoom-Wubah, D. Sun, J. Huang and Q. Li, *J. Chem. Technol. Biotechnol.*, 2015, **90**, 678–685.
67. I. Fierascu, M. I. Georgiev, A. Ortan, R. C. Fierascu, S. M. Avramescu, D. Ionescu, A. Sutan, A. Brinzan and L. M. Ditu, *Sci. Rep.*, 2017, **7**, 12428.
68. N. S. Thakur, J. Bhaumik, S. Kirar and U. C. Banerjee, *ACS Sustainable Chem. Eng.*, 2017, **5**, 7950–7960.
69. D. P. Yang, X. Liu, C. P. Teng, C. Owh, K. Y. Win, M. Lin, X. J. Loh, Y. L. Wu, Z. Li and E. Ye, *Nanoscale*, 2017, **9**, 15753–15759.
70. D. Borah, M. Hazarika, P. Tailor, A. R. Silva, B. Chetia, G. Singaravelu and P. Das, *Appl. Nanosci.*, 2018, **8**, 241–253.
71. S. Sasidharan, R. Poojari, D. Bahadur and R. Srivastava, *ACS Sustainable Chem. Eng.*, 2018, **6**, 10562–10577.
72. M. Klekotko, K. Brach, J. Olesiak-Banska, M. Samoc and K. Matczyszyn, *Mater. Chem. Phys.*, 2019, **229**, 56–60.
73. G. A. Molina, R. Esparza, J. L. Lopez-Miranda, A. R. Hernandez-Martinez, B. L. Espana-Sanchez, E. A. Elizalde-Pena and M. Estevez, *Colloids Surf., B*, 2019, **180**, 141–149.
74. R. Y. Parapat, F. A. Yudatama, M. R. Musadi, M. Schwarze and R. Schomäcker, *Ind. Eng. Chem. Res.*, 2019, **58**, 2460–2470.

75. K. B. Narayanan and N. Sakthivel, *Adv. Colloid Interface Sci.*, 2010, **156**, 1–13.

76. T. J. Park, K. G. Lee and S. Y. Lee, *Appl. Microbiol. Biotechnol.*, 2016, **100**, 521–534.

77. D.-P. Yang, S. Chen, P. Huang, X. Wang, W. Jiang, O. Pandoli and D. Cui, *Green Chem.*, 2010, **12**.

78. R. Selvakumar, N. Seethalakshmi, P. Thavamani, R. Naidu and M. Megharaj, *RSC Adv.*, 2014, **4**, 52156–52169.

79. M. W. Ullah, Z. Shi, X. Shi, D. Zeng, S. Li and G. Yang, *ACS Sustainable Chem. Eng.*, 2017, **5**, 11163–11175.

80. M. Wang, T. Odoom-Wubah, H. Chen, X. Jing, T. Kong, D. Sun, J. Huang and Q. Li, *Nanoscale*, 2013, **5**, 6599–6606.

81. S. K. Das, T. Parandhaman, N. Pentela, A. K. M. Maidul Islam, A. B. Mandal and M. Mukherjee, *J. Phys. Chem. C*, 2014, **118**, 24623–24632.

82. T. Odoom-Wubah, M. Du, W. B. Osei, D. Sun, J. Huang and Q. Li, *Chin. J. Chem. Eng.*, 2015, **23**, 1907–1915.

83. H. Chen, D. Sun, X. Jiang, X. Jing, F. Lu, T. Odoom-Wubah, Y. Zheng, J. Huang and Q. Li, *RSC Adv.*, 2013, **3**.

84. Q. K. Vo, M. N. Nguyen Thi, P. P. Nguyen Thi and D. T. Nguyen, *Processes*, 2019, **7**.

85. W. Lv, C. Gu, S. Zeng, J. Han, T. Jiang and J. Zhou, *Biosensors*, 2018, **8**.

86. L. Wang, C. Hu, Y. Nemoto, Y. Tateyama and Y. Yamauchi, *Cryst. Growth Des.*, 2010, **10**, 3454–3460.

87. X. Wang, D. P. Yang, P. Huang, M. Li, C. Li, D. Chen and D. Cui, *Nanoscale*, 2012, **4**, 7766–7772.

88. J. Zhang, Q. Yu, W. Qiu, K. Li, L. Qian, X. Zhang and G. Liu, *Microchim. Acta*, 2019, **186**, 357.

89. J. Song, S. Hwang, S. Park, T. Kim, K. Im, J. Hur, J. Nam, S. Kim and N. Park, *RSC Adv.*, 2016, **6**, 51658–51661.

90. Z. Wang, J. Zhang, J. M. Ekman, P. J. Kenis and Y. Lu, *Nano Lett.*, 2010, **10**, 1886–1891.

91. Z. Wang, L. Tang, L. H. Tan, J. Li and Y. Lu, *Angew. Chem., Int. Ed.*, 2012, **51**, 9078–9082.

92. H. c. A. Becerril, R. M. Stoltenberg, D. R. Wheeler, R. C. Davis, J. N. Harb and A. T. Woolley, *J. Am. Chem. Soc.*, 2005, **127**, 2828.

93. S. Rudiuk, A. Venancio-Marques, G. Hallais and D. Baigl, *Soft Matter*, 2013, **9**.

94. P. Huang, O. Pandoli, X. Wang, Z. Wang, Z. Li, C. Zhang, F. Chen, J. Lin, D. Cui and X. Chen, *Nano Res.*, 2012, **5**, 630–639.

95. S. Sasidharan, D. Bahadur and R. Srivastava, *ACS Sustainable Chem. Eng.*, 2017, **5**, 10163–10175.

96. S. Sasidharan, D. Bahadur and R. Srivastava, *ACS Appl. Mater. Interfaces*, 2016, **8**, 15889–15903.

97. S. Sasidharan, D. Bahadur and R. Srivastava, *RSC Adv.*, 2016, **6**, 84025–84034.

 98. L. Li and J. Weng, *Nanotechnology*, 2010, **21**, 305603.
 99. X. Ma, Q. Guo, Y. Xie and H. Ma, *Chem. Phys. Lett.*, 2016, **652**, 148–151.
100. T. T. Nhung, Y. Bu and S.-W. Lee, *J. Cryst. Growth*, 2013, **373**, 132–137.
101. T. T. Nhung and S. W. Lee, *ACS Appl. Mater. Interfaces*, 2014, **6**, 21335–21345.
102. N. Ma, X. Liu, Z. Yang, G. Tai, Y. Yin, S. Liu, H. Li, P. Guo and X. S. Zhao, *ACS Sustainable Chem. Eng.*, 2017, **6**, 1133–1140.
103. S. Ouyang, L. Wang, J. Cui, H. Shi, T. Wang and S. Wang, *NANO*, 2015, **10**, 1550106.
104. C. Caucheteur, T. Guo and J. Albert, *Anal. Bioanal. Chem.*, 2015, **407**, 3883–3897.
105. J.-F. Masson, *ACS Sens.*, 2017, **2**, 16–30.
106. K. Y. Tang, J. X. Chen, E. D. R. Legaspi, C. Owh, M. Lin, I. S. Y. Tee, D. Kai, X. J. Loh, Z. Li, M. D. Regulacio and E. Ye, *Chemosphere*, 2021, **265**, 129114.
107. M. Kim, J.-H. Lee and J.-M. Nam, *Adv. Sci.*, 2019, **6**, 1900471.
108. E. Ye, M. D. Regulacio, S. Y. Zhang, X. J. Loh and M. Y. Han, *Chem. Soc. Rev.*, 2015, **44**, 6001–6017.
109. E. Ye, K. Y. Win, H. R. Tan, M. Lin, C. P. Teng, A. Mlayah and M. Y. Han, *J. Am. Chem. Soc.*, 2011, **133**, 8506–8509.
110. M. L. Brongersma, N. J. Halas and P. Nordlander, *Nat. Nanotechnol.*, 2015, **10**, 25–34.
111. G. V. Hartland, L. V. Besteiro, P. Johns and A. O. Govorov, *ACS Energy Lett.*, 2017, **2**, 1641–1653.
112. E. Hao, R. C. Bailey, G. C. Schatz, J. T. Hupp and S. Li, *Nano Lett.*, 2004, **4**, 327–330.
113. H. Yuan, W. Ma, C. Chen, J. Zhao, J. Liu, H. Zhu and X. Gao, *Chem. Mater.*, 2007, **19**, 1592–1600.
114. C. Song, Y. Dou, L. Yuwen, Y. Sun, C. Dong, F. Li, Y. Yang and L. Wang, *J. Mater. Chem. B*, 2018, **6**, 3030–3039.
115. Y. Liu, X. Zhang, L. Luo, L. Li, Y. He, J. An and D. Gao, *ACS Biomater. Sci. Eng.*, 2018, **4**, 2911–2921.
116. H. Moustaoui, J. Saber, I. Djeddi, Q. Liu, A. T. Diallo, J. Spadavecchia, M. Lamy de la Chapelle and N. Djaker, *J. Phys. Chem. C*, 2019, **123**, 17548–17554.
117. Z. Y. Ong, S. Chen, E. Nabavi, A. Regoutz, D. J. Payne, D. S. Elson, D. T. Dexter, I. E. Dunlop and A. E. Porter, *ACS Appl. Mater. Interfaces*, 2017, **9**, 39259–39270.
118. B. Zhang, J. Wang, J. Sun, Y. Wang, T. Chou, Q. Zhang, H. R. Shah, L. Ren and H. Wang, *Adv. Ther.*, 2020, **3**, 2000114.
119. J. Sun, J. Wang, W. Hu, Y. Wang, T. Chou, Q. Zhang, B. Zhang, Z. Yu, Y. Yang, L. Ren and H. Wang, *ACS Appl. Mater. Interfaces*, 2021, **13**, 10778–10795.
120. P. Qiu, M. Yang, X. Qu, Y. Huai, Y. Zhu and C. Mao, *Biomaterials*, 2016, **104**, 138–144.

121. M.-F. Tsai, S.-H. G. Chang, F.-Y. Cheng, V. Shanmugam, Y.-S. Cheng, C.-H. Su and C.-S. Yeh, *ACS Nano*, 2013, **7**, 5330–5342.
122. M. A. Mackey, M. R. K. Ali, L. A. Austin, R. D. Near and M. A. El-Sayed, *J. Phys. Chem. B*, 2014, **118**, 1319–1326.
123. B. Jang, J.-Y. Park, C.-H. Tung, I.-H. Kim and Y. Choi, *ACS Nano*, 2011, **5**, 1086–1094.
124. P. Zijlstra, P. M. R. Paulo and M. Orrit, *Nat. Nanotechnol.*, 2012, **7**, 379–382.
125. C. P. Teng, T. Zhou, E. Ye, S. Liu, L. D. Koh, M. Low, X. J. Loh, K. Y. Win, L. Zhang and M. Y. Han, *Adv. Healthcare Mater.*, 2016, **5**, 2122–2130.
126. M. Bosman, E. Ye, S. F. Tan, C. A. Nijhuis, J. K. W. Yang, R. Marty, A. Mlayah, A. Arbouet, C. Girard and M.-Y. Han, *Sci. Rep.*, 2013, **3**, 1312.
127. Y. Wang, K. C. L. Black, H. Luehmann, W. Li, Y. Zhang, X. Cai, D. Wan, S.-Y. Liu, M. Li, P. Kim, Z.-Y. Li, L. V. Wang, Y. Liu and Y. Xia, *ACS Nano*, 2013, **7**, 2068–2077.
128. P. Huang, P. Rong, J. Lin, W. Li, X. Yan, M. G. Zhang, L. Nie, G. Niu, J. Lu, W. Wang and X. Chen, *J. Am. Chem. Soc.*, 2014, **136**, 8307–8313.
129. X. Li, L. Xing, K. Zheng, P. Wei, L. Du, M. Shen and X. Shi, *ACS Appl. Mater. Interfaces*, 2017, **9**, 5817–5827.
130. Y. Liu, J. R. Ashton, E. J. Moding, H. Yuan, J. K. Register, A. M. Fales, J. Choi, M. J. Whitley, X. Zhao, Y. Qi, Y. Ma, G. Vaidyanathan, M. R. Zalutsky, D. G. Kirsch, C. T. Badea and T. Vo-Dinh, *Theranostics*, 2015, **5**, 946–960.
131. A. Espinosa, A. K. A. Silva, A. Sánchez-Iglesias, M. Grzelczak, C. Péchoux, K. Desboeufs, L. M. Liz-Marzán and C. Wilhelm, *Adv. Healthcare Mater.*, 2016, **5**, 1040–1048.
132. C. Bi, J. Chen, Y. Chen, Y. Song, A. Li, S. Li, Z. Mao, C. Gao, D. Wang, H. Möhwald and H. Xia, *Chem. Mater.*, 2018, **30**, 2709–2718.
133. Y. Pu, Y. Zhao, P. Zheng and M. Li, *Inorg. Chem.*, 2018, **57**, 8599–8607.
134. C. M. Pitsillides, E. K. Joe, X. Wei, R. R. Anderson and C. P. Lin, *Biophys. J.*, 2003, **84**, 4023–4032.
135. V. P. Zharov, J.-W. Kim, D. T. Curiel and M. Everts, *Nanomedicine*, 2005, **1**, 326–345.
136. K. P. Miller, L. Wang, Y.-P. Chen, P. J. Pellechia, B. C. Benicewicz and A. W. Decho, *Front. Microbiol.*, 2015, **6**, 189.
137. J. Z. Zhang, *J. Phys. Chem. Lett.*, 2010, **1**, 686–695.
138. J. B. Vines, J.-H. Yoon, N.-E. Ryu, D.-J. Lim and H. Park, *Front. Chem.*, 2019, **7**, 167.
139. H. R. Moyer and K. A. Delman, *Int. J. Hyperthermia*, 2008, **24**, 251–261.
140. K. H. Luk, R. M. Hulse and T. L. Phillips, *West. J. Med.*, 1980, **132**, 179–185.
141. Q. Zhao, L. Wang, R. Cheng, L. Mao, R. D. Arnold, E. W. Howerth, Z. G. Chen and S. Platt, *Theranostics*, 2012, **2**, 113–121.
142. M. D. Regulacio, D.-P. Yang and E. Ye, *CrystEngComm*, 2020, **22**, 399–411.

143. J. K. Gansel, M. Wegener, S. Burger and S. Linden, *Opt. Express*, 2010, **18**, 1059–1069.
144. N. A. Mirin and N. J. Halas, *Nano Lett.*, 2009, **9**, 1255–1259.
145. L. Jauffred, A. Samadi, H. Klingberg, P. M. Bendix and L. B. Oddershede, *Chem. Rev.*, 2019, **119**, 8087–8130.
146. N. S. Abadeer and C. J. Murphy, *J. Phys. Chem. C*, 2016, **120**, 4691–4716.
147. H. Chen, X. Zhang, S. Dai, Y. Ma, S. Cui, S. Achilefu and Y. Gu, *Theranostics*, 2013, **3**, 633–649.
148. D. H. M. Dam, J. H. Lee, P. N. Sisco, D. T. Co, M. Zhang, M. R. Wasielewski and T. W. Odom, *ACS Nano*, 2012, **6**, 3318–3326.
149. A. S. Patel, S. Juneja, P. K. Kanaujia, V. Maurya, G. V. Prakash, A. Chakraborti and J. Bhattacharya, *Nano-Struct. Nano-Objects*, 2018, **16**, 329–336.
150. C. Gao, J. Vuong, Q. Zhang, Y. Liu and Y. Yin, *Nanoscale*, 2012, **4**, 2875–2878.
151. H. Ma, Z. Liu, Y. Wei and L. Jiang, *Colloids Surf., A*, 2019, **582**, 123889.
152. J. Zhu, M.-J. Liu, J.-J. Li and J.-W. Zhao, *Eur. Phys. J. B*, 2017, **90**, 216.
153. J. l. Li and M. Gu, *IEEE J. Sel. Top. Quantum Electron.*, 2010, **16**, 989–996.
154. P. Wu, Y. Gao, H. Zhang and C. Cai, *Anal. Chem.*, 2012, **84**, 7692–7699.
155. D. Joseph, R. Baskaran, S. G. Yang, Y. S. Huh and Y.-K. Han, *J. Colloid Interface Sci.*, 2019, **542**, 308–316.
156. A. J. McGrath, Y.-H. Chien, S. Cheong, D. A. J. Herman, J. Watt, A. M. Henning, L. Gloag, C.-S. Yeh and R. D. Tilley, *ACS Nano*, 2015, **9**, 12283–12291.
157. H.-C. Lin, K.-F. Hsu, C.-L. Lai, T.-C. Wu, H.-F. Chen and C.-H. Lai, *Molecules*, 2020, **25**.
158. A. Bassegoda, K. Ivanova, E. Ramon and T. Tzanov, *Appl. Microbiol. Biotechnol.*, 2018, **102**, 2075–2089.
159. L. Hall-Stoodley, J. W. Costerton and P. Stoodley, *Nat. Rev. Microbiol.*, 2004, **2**, 95–108.
160. R. Smith and J. Coast, *Br. Med. J.*, 2013, **346**, f1493.
161. R. Weissleder, *Nat. Biotechnol.*, 2001, **19**, 316–317.
162. J. Olson, S. Dominguez-Medina, A. Hoggard, L.-Y. Wang, W.-S. Chang and S. Link, *Chem. Soc. Rev.*, 2015, **44**, 40–57.
163. A. N. S. Insitute, Washington, 2005, vol. ANSI-Z136.3.
164. A. O'Toole, E. B. Ricker and E. Nuxoll, *Biofouling*, 2015, **31**, 665–675.
165. V. P. Zharov, K. E. Mercer, E. N. Galitovskaya and M. S. Smeltzer, *Biophys. J.*, 2006, **90**, 619–627.
166. N. W. S. Kam, M. Connell, J. A. Wisdom and H. Dai, *Proc. Natl. Acad. Sci. U. S. A.*, 2005, **102**, 11600.
167. X. Li, S. M. Robinson, A. Gupta, K. Saha, Z. Jiang, D. F. Moyano, A. Sahar, M. A. Riley and V. M. Rotello, *ACS Nano*, 2014, **8**, 10682–10686.
168. P. Yuan, X. Ding, Z. Guan, N. Gao, R. Ma, X.-F. Jiang, Y. Y. Yang and Q.-H. Xu, *Adv. Healthcare Mater.*, 2015, **4**, 674–678.
169. V. Knittel, M. P. Fischer, T. de Roo, S. Mecking, A. Leitenstorfer and D. Brida, *ACS Nano*, 2015, **9**, 894–900.

AQ:15

170. S. Freddi, L. Sironi, R. D'Antuono, D. Morone, A. Donà, E. Cabrini, L. D'Alfonso, M. Collini, P. Pallavicini, G. Baldi, D. Maggioni and G. Chirico, *Nano Lett.*, 2013, **13**, 2004–2010.

171. M. Borzenkov, M. Moros, C. Tortiglione, S. Bertoldi, N. Contessi, S. Fare, A. Taglietti, A. D'Agostino, P. Pallavicini, M. Collini and G. Chirico, *Beilstein J. Nanotechnol.*, 2018, **9**, 2040–2048.

172. P. Pallavicini, A. Donà, A. Taglietti, P. Minzioni, M. Patrini, G. Dacarro, G. Chirico, L. Sironi, N. Bloise, L. Visai and L. Scarabelli, *Chem. Commun.*, 2014, **50**, 1969–1971.

173. J. Penders, M. Stolzoff, D. J. Hickey, M. Andersson and T. J. Webster, *Int. J. Nanomed.*, 2017, **12**, 2457–2468.

174. J. Wang, J. Zhang, K. Liu, J. He, Y. Zhang, S. Chen, G. Ma, Y. Cui, L. Wang and D. Gao, *Int. J. Pharm.*, 2020, **580**, 119231.

175. X. Jiang, X. Fan, W. Xu, R. Zhang and G. Wu, *ACS Biomater. Sci. Eng.*, 2020, **6**, 680–689.